

# Non-monotonic variation with salt concentration of the second virial coefficient in protein solutions

E. Allahyarov<sup>1</sup>, H. Löwen<sup>2</sup>, J.P. Hansen<sup>3</sup>, and A.A. Louis<sup>3</sup>

<sup>1</sup>*Institut für Festkörperforschung, Forschungszentrum Jülich, D-52425 Jülich, Germany*

<sup>2</sup>*Institut für Theoretische Physik II, Heinrich-Heine-Universität Düsseldorf, D-40225 Düsseldorf, Germany*

<sup>3</sup>*Department of Chemistry, Lensfield Rd, Cambridge CB2 1EW, UK*

## Abstract

The osmotic virial coefficient  $B_2$  of globular protein solutions is calculated as a function of added salt concentration at fixed pH by computer simulations of the “primitive model”. The salt and counter-ions as well as a discrete charge pattern on the protein surface are explicitly incorporated. For parameters roughly corresponding to lysozyme, we find that  $B_2$  first decreases with added salt concentration up to a threshold concentration, then increases to a maximum, and then decreases again upon further raising the ionic strength. Our studies demonstrate that the existence of a discrete charge pattern on the protein surface profoundly influences the effective interactions and that non-linear Poisson Boltzmann and Derjaguin-Landau-Verwey-Overbeek (DLVO) theory fail for large ionic strength. The observed non-monotonicity of  $B_2$  is compared to experiments. Implications for protein crystallization are discussed.

PACS: 82.70.Dd, 61.20.Qg, 87.15.Aa

## I. INTRODUCTION

Interactions between proteins in aqueous solutions determine their collective behavior, in particular their aggregation, their complexation with other macromolecules, and ultimately their phase behavior, including phase separation, precipitation and crystallization. Any theoretical analysis of the properties of protein solutions must rely on a reliable understanding of their interactions. A good example is provided by the control of protein crystallization, which is an essential prerequisite for the determination of protein structure by X-ray diffraction [1,2]. While at present protein crystallization is still mostly achieved experimentally by “trial and error”, and on the basis of a number of empirical rules [3], there is clearly a need for a more fundamental understanding of the mechanisms controlling protein crystallization, and this obviously requires a good knowledge of the forces between protein molecules in solution, and of their dependence on solution conditions, including pH and salt concentration [1,4–6].

Protein interactions have various origins, and one may conveniently distinguish between direct and induced (or effective) contributions. Direct interactions include short-range repulsive forces, which control steric excluded volume effects, reflecting the shape of the protein, van der Waals dispersion forces, and electrostatic forces associated with pH-dependent electric charges and higher electrostatic multipoles carried by the protein residues [7]. Other, effective, interactions depend on the degree of coarse-graining in the statistical description and result from the tracing out of microscopic degrees of freedom associated with the solvent and added electrolyte, i.e. the water molecules and microions. Tracing out the solvent results in hydrophobic attraction and hydration forces, while integrating over microion degrees of freedom leads to screened electrostatic interactions between residues, the range of which is controlled by the Debye screening length, and hence by electrolyte concentration.

However, while coarse-graining through elimination of microscopic degrees of freedom, leading to state-dependent effective interactions is a priori a reasonable procedure to describe highly asymmetric colloidal systems, where particles have diameters of typically hundreds

of nm and carry thousands of elementary charges, this is obviously less justified for the much smaller and less charged proteins. In particular the assumption of uniformly charged colloid surfaces, leading to spherically symmetric, screened interactions between the electric double layers around colloid particles, as epitomized by the classic DLVO (Derjaguin-Landau-Verwey-Overbeek) potential [8], ceases to be a reasonable approximation at the level of nanometric proteins carrying typically of order 10 elementary charges. The reason is that length scales which are widely separated in colloidal assemblies, become comparable in protein solutions, while the discreteness of charge distributions on proteins can no longer be ignored, since the distance between two charged residues on the protein surface is no longer negligible compared to the protein diameter. Thus, electrostatic, as well as other (e.g. hydrophobic) interactions are much more specific in proteins, and must be associated with several interaction sites, rather than merely with the centers of mass as is the case for (spherical) colloidal particles.

Another very important distinction between colloids and protein solutions is that the forces between the former may be measured directly, using optical means [9–11], while interactions between proteins can only be inferred indirectly, from measurements by static light scattering of the osmotic equation of state which, at sufficiently low concentrations, yields the second osmotic virial coefficient  $B_2$  [3,12–14], the main focus of the present paper. The variation of  $B_2$  with solution conditions yields valuable information on the underlying effective pair interactions between proteins. Moreover it was shown empirically by George and Wilson [3] that there is a strong correlation between the measured values of  $B_2$  and the range of solution conditions which favor protein crystallization [12,15,16]. Only if the measured value of  $B_2$  falls within a well defined “slot” can crystallization be achieved. If  $B_2$  is too large, repulsive interactions predominate, leading to slow crystallization rates. On the other hand if  $B_2$  is highly negative, strong attractions lead to amorphous aggregation.

The correlation between  $B_2$  and crystallization may be rationalized by noting that protein crystals generally coexist with a fairly dilute protein solution, the thermodynamic properties (and in particular the free energy) of which are essentially determined by  $B_2$ . Coexistence

between a dense solid phase and a dilute fluid phase is generally a signature of a very short-ranged attraction between particles as compared to their diameter [16–19].

For such short-ranged attractive interactions, the phase-separation into dilute and concentrated proteins solutions expected on the basis of a mean-field, van der Waals theory, is in fact pre-empted by the freezing transition, i.e. the critical (or “cloud”) point lies below the freezing line. The critical fluctuations associated with this metastable cloud point may lead to a significant enhancement of the crystal nucleation rate [20], while the position of the cloud point in the concentration-temperature plane is strongly correlated with the virial coefficient  $B_2$  [16].

The present paper focuses on the variation of  $B_2$  with ionic strength of added salt. This is a particularly important issue since “salting out” of protein solutions is one of the standard methods used to induce crystallization. An increase in salt concentration reduces the screening length and hence the electrostatic repulsion, allowing short range attractive forces (e.g. of hydrophobic or van der Waals origin) to come into play which will ultimately trigger nucleation. Recent experiments point to a non-monotonic variation of  $B_2$  with increasing ionic strength [21,22], or to a pronounced shoulder in the  $B_2$  versus ionic strength curve [23] in lysozyme solutions. Closely related findings are the observation of a non-monotonic cloud point [24–26], and of a minimum in the solubility of lysozyme with increasing salt concentration [27]; the solubility is obviously related to the osmotic virial coefficient [28]. Similarly, the attractive interaction parameter  $\lambda$ , which controls the variation of the measured protein diffusion coefficient  $D$  with volume fraction, was found to exhibit a sharp minimum upon an increase of ionic strength of lysozyme solutions [29]; again, this interaction parameter strongly correlates with  $B_2$  [30,31].

Traditional models for the protein–protein interaction cannot easily reproduce such non-monotonic behavior of  $B_2$  or related quantities. The “colloidal” approach based on spherical particles interacting via the screened Coulomb DLVO potential [8] can only predict a monotonic decrease of  $B_2$  with ionic strength [5,32]. The same is true of models [5,12,15] accounting for short-range attractions via Baxter’s “adhesive sphere” representation [33]. In

these models, which assume central pair-wise interactions,  $B_2$  reduces to a simple integral of the Mayer function associated with the spherically symmetric potential [34,35]. More recent calculations account for the asymmetric shape of proteins [22,36], or include several “sticky” sites at the surface of the protein [37,38].

In these traditional calculations, electrostatic interactions between proteins and microions are routinely treated within mean-field Poisson-Boltzmann (PB) theory, generally in its linearized version (as is the case for the classic DLVO potential). However, as explained earlier, all relevant length scales (i.e. protein diameter, mean distance between charged sites on the protein surface, and between co and counterions, as well as the Debye screening length) are comparable in protein solutions, so that the discrete nature of both the interaction sites, and of the co and counterions, can no longer be ignored. Moreover, Coulomb correlations are expected to be enhanced on protein length scales and may lead to strong deviations from the predictions of PB theory, which have recently been shown to induce short-range attractions, even between much larger colloidal particles [24,39–42].

The present paper takes into account the discrete nature of the microions within a “primitive model” description of the electrolyte, and presents results of Molecular Dynamics calculations of the equilibrium distribution of co and counterions around two proteins and of the resulting osmotic virial coefficient  $B_2$ . Two models of the charge distribution on the surface of the spherical proteins will be considered. In the colloid-like model the charge is assumed to be uniformly distributed over the surface, while in the discrete charge model, the charges are attached to a small number of interaction sites. The latter model will be shown to lead to a distinctly non-monotonic variation of  $B_2$  with ionic strength, as observed experimentally.

The paper is organized as follows: The model and key physical quantities are introduced in section II. Simulation details are described in section III. Results of the simulations are presented and discussed in section IV, while conclusions are summarized in section V. A preliminary account of parts of the results was briefly reported elsewhere [43].

## II. MODELS, EFFECTIVE FORCES AND SECOND VIRIAL COEFFICIENT

The globular proteins under consideration are modeled as hard spheres of diameter  $\sigma_p$ , carrying a total (negative) charge  $-Ze$ . Within a “primitive model” representation [44], the molecular granularity of the aqueous solvent is ignored, and replaced by a continuum of dielectric permittivity  $\epsilon$ , while the monovalent counterions and salt ions are assumed to have equal diameters  $\sigma_s$  and charges  $\pm e$ .

Two models are considered for the charge distribution on the surface of the protein. In the “smeared charge model” (SCM), the total charge  $-Ze$  is assumed to be uniformly distributed over the spherical surface, which is the standard model for charge-stabilized colloidal suspensions [24,39–42], involving highly charged objects. According to Gauss’ theorem, the SCM is equivalent to the assumption that the total charge  $Ze$  is placed at the center of the sphere. In the “discrete charge model” (DCM), point charges ( $-e$ ) are distributed over a sphere of diameter  $\sigma_d = \alpha\sigma_p$  (with  $\alpha < 1$ , i.e. slightly inside the protein surface), in such a way as to minimize the electrostatic energy of the distribution. The resulting charge pattern, well known from the classic Thompson problem (see [47] for a recent review), is kept fixed throughout. Such Thompson patterns do not correspond to the true charge distribution on any specific protein (see [45,46] where a simple toy model of lysozyme with different charge ditribution corresponding to solutions of different pH is constructed) but do provide a well defined discrete model for any value of  $Z$ . Note that the discrete distributions are characterized by non-vanishing multi-pole moments, depending on the symmetry of the distribution for any specific value of  $Z$ , while the SCM implies vanishing multipoles of all orders.

At this stage the SCM and DCM models involve only excluded volume and bare Coulomb interactions (reduced by a factor  $1/\epsilon$  to account for the solvent) between all particles, proteins as well as microions.

The following physical quantities were systematically computed in the course of the MD simulations, to be described in the following section.

**a)** the density profiles of co and counterions around a single globular protein

$$\rho_{\pm}(r) = \langle \sum_j \delta(\vec{r}_j^{\pm} - \vec{r}) \rangle \quad (1)$$

Here  $\vec{r}_j^{\pm}$  is the position of the  $j^{th}$  microion of species  $\pm$  relative to the protein center, while the angular bracket denotes a canonical average over the microion configurations. For an isolated SCM protein these profiles are spherically symmetric, and depend only on the radial distance  $r = |\vec{r}|$ . For isolated DCM proteins the profiles are no longer spherically symmetric, and may be expanded in spherical harmonics, as discussed in the Appendix. The anisotropy turns out to be weak, and only the spherically symmetric component (corresponding to averaging  $\rho_{\pm}(\vec{r})$  over protein orientations) will be shown in the following.

**b)** The second quantity, which will be the key input in the calculation of  $B_2$ , is the microion averaged total force  $\vec{F}_1 = -\vec{F}_2$  acting on the center of two proteins, placed at a relative position  $\vec{r} = \vec{r}_1 - \vec{r}_2$ ; the force  $\vec{F}_1$  is a function of  $\vec{r}$ . Its statistical definition was discussed earlier in the context of charged colloids [39,48,49], and it involves three contributions:

$$\vec{F}_1 = \vec{F}_1^{(1)} + \vec{F}_1^{(2)} + \vec{F}_1^{(3)}. \quad (2)$$

$\vec{F}_1^{(1)}$  is the direct Coulomb repulsion between the charge distributions on the two proteins;  $\vec{F}_1^{(2)}$  is the microion induced electrostatic force, while  $\vec{F}_1^{(3)}$  is the depletion force which may be traced back to the in-balance of the osmotic pressure of the microions acting on the opposite sides of protein 1 due to the presence of protein 2.  $\vec{F}_1^{(3)}$  is directly expressible as the integral of the microion contact density over the surface of the protein [50,51].

In the case of the SCM, the microion averaged force depends only on the distance  $r = |\vec{r}_{12}|$  between the two proteins. For the DCM, on the other hand,  $\vec{F}_1$  is a function of the relative orientations of the two proteins, as characterized by the sets of Euler angles  $\vec{\Omega}_1$  and  $\vec{\Omega}_2$ , i.e.  $\vec{F}_1 = \vec{F}_1(\vec{r}, \vec{\Omega}_1, \vec{\Omega}_2)$ .

**c)** Once the force  $\vec{F}_1$  has been determined as a function of  $\vec{r}$ ,  $\vec{\Omega}_1$  and  $\vec{\Omega}_2$ , one may then calculate an orientationally averaged, but distance resolved, effective protein-protein pair potential according to

$$V(r) = \int_r^\infty dr' \left\langle \frac{\vec{r}'}{|\vec{r}'|} \cdot \vec{F}_1(\vec{r}', \vec{\Omega}_1, \vec{\Omega}_2) \right\rangle_{\vec{\Omega}_1, \vec{\Omega}_2}. \quad (3)$$

where the angular brackets  $\langle \dots \rangle_{\vec{\Omega}_1, \vec{\Omega}_2}$  refer to a canonical statistical average over mutual orientations of the two proteins weighted by the Boltzmann factor of the effective potential  $V_{eff}(\vec{r}, \vec{\Omega}_1, \vec{\Omega}_2)$  such that  $\partial V_{eff}(\vec{r}, \vec{\Omega}_1, \vec{\Omega}_2)/\partial \vec{r} = -\vec{F}_1(\vec{r}, \vec{\Omega}_1, \vec{\Omega}_2)$ . Explicitly, for any quantity  $A(\vec{r}, \vec{\Omega}_1, \vec{\Omega}_2)$ ,

$$\langle A \rangle_{\vec{\Omega}_1, \vec{\Omega}_2} = \frac{\int d\vec{\Omega}_1 d\vec{\Omega}_2 A(\vec{r}, \vec{\Omega}_1, \vec{\Omega}_2) \exp\{(-V_{eff}(\vec{r}, \vec{\Omega}_1, \vec{\Omega}_2)/k_B T)\}}{\int d\vec{\Omega}_1 d\vec{\Omega}_2 \exp\{-V_{eff}(\vec{r}, \vec{\Omega}_1, \vec{\Omega}_2)/k_B T\}} \quad (4)$$

d) The second virial coefficient  $B_2$  finally follows from the expression

$$B_2 = \frac{1}{2} \int d\vec{r} [1 - b(r)] \quad (5)$$

where

$$b(r) = \left(\frac{1}{8\pi^2}\right)^2 \int d\vec{\Omega}_1 d\vec{\Omega}_2 \exp(-V_{eff}(\vec{r}, \vec{\Omega}_1, \vec{\Omega}_2)/k_B T). \quad (6)$$

The angular integrations are trivial in the case of the SCM, where  $V_{eff}$  depends on  $r$ . In the case of the DCM, one may use the identity

$$b(r) = \exp \left[ - \int_r^\infty dr' \frac{d}{dr'} [\ln b(r')] \right], \quad (7)$$

to show that  $B_2$  may be cast in a form similar to that appropriate for the SCM, namely

$$B_2 = \frac{1}{2} \int d\vec{r} [1 - \exp\{-V(r)/k_B T\}] \quad (8)$$

where  $V(r)$  is the potential of the orientationally averaged projected force, as defined in Eq. (3). As pointed out earlier,  $B_2$  is directly accessible experimentally by extrapolating light scattering data to small wavevectors [35] or by taking derivatives of osmotic pressure data with respect to concentration [13,14]. Results will be presented in the form of the reduced second virial coefficient  $B_2^* = B_2/B_2^{(HS)}$  where  $B_2^{(HS)} = 2\pi\sigma_p^3/3$ , i.e.

$$B_2^* = 1 + \frac{3}{\sigma_p^3} \int_{\sigma_p}^\infty r^2 dr [1 - \exp\{-V(r)/k_B T\}]. \quad (9)$$



### III. SIMULATION DETAILS

We study a pair ( $N_p = 2$ ) of spherical proteins with center-to-center separation  $r$ , confined in a cubic box of length  $L = 4\sigma_p$ , which also contained monovalent co and counterions in numbers determined by their bulk concentrations and overall charge neutrality. There are  $ZN_p$  counterions dissociated from the protein surface, and added  $N_s$  salt ion pairs such that the screening of proteins is implemented via  $N_+ = N_s$  coions and  $N_- = N_s + ZN_p$  counterions in simulation box. A snapshot of a typical equilibrium microion configuration around two proteins is shown in Figure 1 for the protein charge number  $Z = 15$ . The two proteins were placed symmetrically with respect to the center along the body diagonal of a cubic simulation cell; periodic boundary conditions in three dimensions were adopted.  $L$  was chosen such that the box length is much larger than the range of the total (effective) protein-protein interaction, so that the results are independent of  $L$  for non-zero salt concentration. The long-range electrostatic interactions between two charged particles in the simulation box with periodic boundary conditions were modified using the Lekner summation method of images [52]. For our model to be a rough representation of lysozyme, we chose  $\sigma_p = 4nm$ , and three different protein charges  $Z = 6, 10$  and  $15$ , corresponding to three different values of the solution pH. The microion diameter is fixed to be  $\sigma_c = \sigma_p/15 = 0.267nm$ .

For both the SCM and the DCM, the contact coupling parameter between a protein and a microion, namely  $\Gamma = 2e^2/[\epsilon k_B T(\sigma_p - \sigma_d + \sigma_c)]$  for the DCM, and  $\Gamma = 2Ze^2/[\epsilon k_B T(\sigma_p + \sigma_c)]$  for the SCM, are comparable, and of the order of  $\Gamma \approx 3$  at room temperature. We fixed the dielectric constant of water to be  $\epsilon = 81$  and the system temperature to be  $T = 298K$ . Varying salt concentration for fixed protein charge  $Z$  corresponds to a fixed solution pH [53].

Details of the runs corresponding to different salt concentrations are summarized in Table I. Note that the Debye screening length  $r_D$ , defined by

$$r_D = \sqrt{\frac{\epsilon k_B T V'}{8\pi(N_s + Z)q_s e^2}}, \quad (10)$$

is less than  $10\text{\AA}$  for salt concentration beyond 0.1M. Here

$$V' = V - \frac{\pi N_p}{6}(\sigma_p^3 + \sigma_c^3), \quad (11)$$

is the accessible volume for salt ions such that the salt concentration  $C_s$  is  $N_s/V'$ . Thus, the point charges on the protein surface are effectively screened from each other [25]. For each of the runs indicated in Table I, the distance-resolved effective forces and interaction potentials are calculated according to Eqs. (2,3). The statistical averages over microion configurations leading to  $\vec{F}_1^{(2)}$  and  $\vec{F}_1^{(3)}$  were evaluated from time averages in the Molecular Dynamics (MD) simulations.

#### IV. MICROION DISTRIBUTIONS AROUND A SINGLE PROTEIN

First, as a reference, consider a single protein ( $N_p = 1$ ) placed at the center of the simulation box. We calculated spherically averaged, radial microion density profiles  $\rho(r) = \rho_+(r) + \rho_-(r)$  in the immediate vicinity of the protein surface. For a single *neutral* sphere in a salted solution, results for  $\rho(r)$  are drawn in Figure 2. There is a marked depletion in the microion density, signaled by a minimum of  $\rho(r)$ , well below the asymptotic bulk value. The depletion is enhanced upon increasing the salt concentration. At sufficiently high salt concentrations, this minimum is followed by a weak, but detectable, ion layer (see corresponding lines for runs 7 and 9 in Figure 2). The formation of a depletion zone is *not* a consequence of the direct (hard core) interaction between salt ions and the protein surface, since the position of the observed layer is significantly further away from the protein surface than one ion diameter. A rough estimate for the distance between layer and neutral sphere gives a value of  $2.5\sigma_s$ , or equivalently  $0.17\sigma_p$ . For runs 7 and 9, where the ion layer emerges, this distance is of the order of an average ion separation  $r_s$  in the system and twice the Debye screening length  $r_D$  as well (see Table I). Obviously, it is the small ion correlations which lead to the peak formation in the salt density profiles. As an intuitive argument, we posit that the lack of mutual polarization in dense salt solution near neutral surfaces causes the ion depletion. Qualitatively similar depleted density profiles were observed in Lennard-Jones system confined between neutral planes [54] and in Yukawa mixtures [55].

Furthermore, an effective force that pushes a single ion toward regions of higher salinity is predicted within Debye-Hückel theory for interfacial geometries [56].

Next we consider a protein sphere with charge number  $Z = 10$ . The density profiles of small ions are shown in Figure 3 for both the SCM and DCM. Figure 4 represents the corresponding total salt densities, as a sum of co- and counterion densities from Figure 3. At the lower salt concentration (up to run 5) the SCM and DCM models both yield an accumulation of the microion density near ion-protein contact, in semi-quantitative agreement with the prediction of standard Poisson-Boltzmann (PB) theory. For rising ionic strength the total microion density gets depleted near the protein surfaces, as in the previously considered case of a neutral sphere. Remarkably, this depletion occurs both with the SCM and DCM and contradicts the PB prediction. The intuitive picture is that a microscopic layer of counterions is formed around the proteins. An additional salt pair now profits more from the bulk polarization than from the protein surface polarization and is thus excluded from this layer. By normalizing the profiles to the total bulk density, this effect becomes visible as a depletion zone in Figure 4, where a noticeable difference between the SCM and DCM profiles also emerges. Whereas the DCM predicts a contact value  $\rho_c(r = (\sigma_p + \sigma_c)/2)$  larger than the bulk value, SCM predicts a much stronger microion depletion near contact. Together with this, the contact value of the DCM model is always larger than that of the SCM model for the same salt concentrations. This finding illustrates the sensitivity of correlation effects to the assumed charge pattern at the surface of a protein. This correlation effect is, of course, absent in the (non-linear) PB and DLVO theories, which always predict a monotonically decreasing density profile  $\rho(r)$  (see Figure 5). Within DLVO theory the density of plus and minus salt ions near protein surface in the SCM model are defined as

$$\begin{aligned}\rho_+(r) &= -\frac{Z_{DLVO}}{q_s} \frac{k_+^2}{4\pi} \frac{e^{-k_D r}}{r} + \frac{2\bar{\rho}_+ \bar{\rho}_-}{\bar{\rho}_+ + \bar{\rho}_-}, \\ \rho_-(r) &= \frac{Z_{DLVO}}{q_s} \frac{k_+^2}{4\pi} \frac{e^{-k_D r}}{r} + \frac{2\bar{\rho}_+ \bar{\rho}_-}{\bar{\rho}_+ + \bar{\rho}_-}.\end{aligned}\tag{12}$$

where

$$\begin{aligned} \bar{\rho}_+ &= \frac{N_s + 2Z}{V'}, \quad \bar{\rho}_- = \frac{N_s}{V'}, \quad Z_{DLVO} = Z \frac{\exp(k_D \sigma_p/2)}{1 + k_D \sigma_p/2}, \\ k_D^2 &= k_+^2 + k_-^2, \quad k_-^2 = 4\pi q_s^2 e^2 \bar{\rho}_- / \epsilon k_B T, \quad k_+^2 = 4\pi q_s^2 e^2 \bar{\rho}_+ / \epsilon k_B T. \end{aligned} \quad (13)$$

Nonlinear PB equations were solved via iterations of the potential of a homogeneously charged sphere placed at the center of a spherical cell. The cell radius was determined by the given protein concentration.

A direct comparison between SCM, DCM models and non-linear PB theory is shown in Fig. 6 for two of the higher salt concentrations from Fig. 4. For the intermediate salt concentration  $C_s = 0.206$  Mol/l (run 4) both simulation and theory predict a monotonic decrease of salt density away from the protein surface, whereas, in the case of a dense salt,  $C_s = 0.824$  Mol/l (run 7), simulation results strongly deviate from the PB prediction.

A multipole expansion of the total salt number density in the DCM, discussed in Appendix A, demonstrates that the higher order expansion coefficients are strongly damped and much weaker than the zero-order homogeneous term shown in Figs. 3, 4 and 6.

### A. Effective force and $B_2$ for a protein pair

Next we calculate the angularly averaged effective interaction force  $F(r) = -\frac{dV(r)}{dr}$  and potential  $V(r)$  between two proteins embedded in a sea of small salt ions. Simulation results for the simpler case of the SCM, are plotted in Figure 7 for  $Z = 10$  and compared to the DLVO predictions. There is a systematic deviation between the theoretical and simulation results. While the DLVO theory [8] potential

$$U^{(DLVO)}(r) = \frac{Z_{DLVO}^2 e^2}{\epsilon r} \exp(-r/r_D), \quad (14)$$

always results in repulsive forces, simulations indicate the possibility of an attraction between proteins for large salt concentrations. The force  $F(r)$  at the higher salt concentrations  $C_s$ , shows a maximum at a distance  $r$  nearly equal to the ion diameter. Note that, for the highest salt concentration considered,  $C_s = 2.061$  Mol/l (run 11), where the electrostatic interactions are almost completely screened out, the effective force  $F(r)$  is dominated by

entropic effects; it is reminiscent of entropic depletion force of hard sphere system. The corresponding potential is negative at short distances as shown in the inset of Figure 7, and is related to the depletion in the microion total density profiles  $\rho(r)$  around an isolated protein, shown in Figure 4. We note that such an entropic attraction is not contained in DLVO theory. Its origin is also different from the salting out effect studied in [12,57–60] or the macroion overcharging effect studied in [61]. In Figure 8 the salt dependence of the total interaction force  $F(r)$  (Eq.(2)) is broken down into its components  $F^{(2)}$  and  $F^{(3)}$  for two values of  $r$ . This helps to show that at large salt concentrations, it is indeed the entropic component that causes the force to be attractive for run 11 in Figs 7 and 8a. Finally, we mention that the range of attraction observed here will depend on the electrolyte (salt ion) size. This feature of our model may hint at a cause for the salt specificity observed in salting out experiments on protein crystallization [62]. In addition, as shown in [63], an entropic attraction from the electrolyte could lead even to phase separation in colloid-electrolyte mixtures. Including this term leads to an effective Hamaker constant – describing the dispersion interactions – that is lower, and in better accord with experimental findings [2,64].

The same calculations were carried out for the other two protein charges for the SCM model,  $Z = 6$  and  $Z = 15$ , with qualitatively similar results to those obtained for  $Z = 10$ .

It is clear that the effective forces and potentials between two proteins will no longer be spherically symmetric within the DCM model. For example, three distinguishable mutual orientations of the two proteins are schematically outlined in Figure 9a, corresponding to particular configurations of the Euler angles  $\vec{\Omega}_1, \vec{\Omega}_2$  of the two proteins. Nevertheless, our simulation results, presented in Figure 9b, for the three orientations, show that the actual anisotropy of force is weak. However, this is no longer true for the Yukawa segment model [49,65,66], as shown in the inset of Figure 9b. Within this model, the total effective interaction potential between a pair of protein spheres is given by

$$U^{(YS)}(r) = \frac{1}{Z^2} \sum_{k,n=1}^Z U^{(DLVO)}(|\vec{r}_k - \vec{r}_n|), \quad (15)$$

where  $\vec{r}_k$  and  $\vec{r}_n$  represent the positions of the point unit charges of different proteins. We emphasize that the aelotopic (or nonisotropic) interactions incorporated in our DCM differ from those considered, for example, in Ref. [38], where  $B_2$  is calculated for a set of hydrophobic *attractive* patches on protein surface. Within our version of the DCM the third configuration in Fig. 9 (solid line), has the highest statistical weight of the three cases pictured (see Eqs.(3,4)). If, on the other hand, the point charges on the protein are replaced by attractive patches [38], then the configuration with two points nearly touching (dot-dashed line in Figure 9), is the statistically most favorable conformation. Similar arguments hold within a molecular model for site-specific short-range attractive protein-protein interactions, [67,68]. Results for distance-resolved forces within the DCM model are shown in Figure 10a, for  $Z = 10$ . When the salt concentration is less than  $C_s \lesssim 0.2$  Mol/l, the results are similar to those of the SCM model: i.e. for low ionic strength, the force is repulsive, while for high ionic strength there is an attraction near contact followed by a repulsive barrier. The distinguishing property of the DCM is the *nonmonotonicity* of the force with the increase of ionic strength. This, in turn, gives rise to the nonmonotonic behavior of the spherically averaged interaction potential  $V(r)$  shown in Figure 10b. This feature of  $V(r)$  manifests itself in the following way in Figure 10b: the potential is first strongly reduced as  $C_s$  is increased, then its amplitude and range increase very significantly at intermediate concentrations ( $C_s \simeq 1$  Mol/l), before it nearly vanishes at the highest salt concentrations. Note that  $V(r)$  even becomes slightly attractive at contact ( $r = \sigma_p$ ) for  $C_s \simeq 2$  Mol/l. Similar effects are also observed for  $Z = 6$  and  $Z = 15$  (see Figure 11), suggesting that the effect is generic for discrete charge distributions.

Once the effective potential  $V(r)$  is known, it is straightforward to calculate the second osmotic virial coefficient using Eq.(8). In doing so, however, one should keep in mind that it is the total interaction that enters  $B_2$ . Real proteins also exhibit an additional short-range interaction, as seen, for example, in experimental studies of the osmotic pressure and structural data for lysozyme [69], or in fits to its phase-behavior [15]. This attraction stems from hydration forces, van-der-Waals interactions, and other molecular interactions that

are, to a first approximation, independent of salt concentration. Hence, we have taken the expected short-range attraction between proteins into account by adding to the effective Coulomb potential in Eq.(9), an additional “sticky” sphere potential of the Baxter form [33],

$$\frac{V_{SHS}(r)}{k_B T} = \begin{cases} \infty & r \leq \sigma_p \\ \ln \left[ \frac{12\tau\delta}{\sigma_p + \delta} \right] & \sigma_p < r < \sigma_p + \delta, \\ 0 & r \geq \sigma_p + \delta \end{cases} \quad (16)$$

with potential parameters  $\delta = 0.02\sigma_p$  and  $\tau = 0.12$ , which yield reasonable osmotic data for lysozyme solutions [15,23,69] in the high salt concentration regime. This square well potential is isotropic by nature and ignores the directionality in hydrophobic attraction between proteins [28,37]. Short range attractions lead to “energetic fluid” behavior [70], where the crystallization is driven primarily by the details of the interactions, instead of being dominated by the usual entropic hard-core exclusions. This suggests that the directionality may be very important to details of the protein crystallization behavior [37]. However, for the physically simpler behavior of the virial coefficient, the directionality can be ignored as a first approximation. For simplicity, we assume the parameter  $\tau$  to be independent of electrolyte conditions, although a weak dependence based on experimental observations is reported in [23,68]. The addition of  $V_{SHS}(r)$  strongly magnifies the nonmonotonicity of  $B_2$  stemming from the nonmonotonic behavior of  $V(r)$  near contact.

Results for  $B_2^*$  as a function of salt concentration are shown in Figure 12 for three different protein charges. There is a considerable *qualitative* difference between the predictions of the SCM and the DCM models for the variation of  $B_2^*$  with monovalent salt concentration  $C_s$  for each protein charge  $Z$ . Whereas the SCM (dashed curves in Figure 12) predicts a monotonic decay of  $B_2^*$  with  $C_s$ , the DCM leads to a markedly non-monotonic variation, involving an initial decay toward a minimum (salting-out) followed by a subsequent increase to a maximum (salting-in) and a final decrease at high  $C_s$  values (salting-out). The location of the local minima shifts to higher/lower values of  $C_s$  for larger/smaller protein charges  $Z$ . Thus for larger protein charge one needs a higher salt concentration to achieve the

“salting out” conditions conducive to protein crystallization [35]. Even though the effective Coulomb potential between proteins is small, with an amplitude only a few percent of the thermal energy  $k_B T$ , its effect on  $B_2$  is dramatically enhanced by the presence of the strong short-range attractive Baxter potential.

We have also compared the effective potentials shown in figure 12 with a recently proposed scaling collapse of protein osmotic virial coefficients [35]. This scaling effect, observed for a number of experimental conditions [35], can be explained with simple arguments based on Donnan equilibrium [71]. To lowest order, the effects of salt concentration and protein charge on  $B_2$  are to subsume in the following approximate scaling relation:

$$B_2^{(0)} = B_2 - Z^2/4C_s, \quad (17)$$

where  $B_2^{(0)}$  is the bare virial coefficient, independent of charge effects. As shown, for example in Figure 1 of reference [71], this simple relation holds remarkably well above a salt concentration of  $C_s \approx 0.25M$  for a wide range of experimental measurements of  $B_2$  for lysozyme, which all tend to a plateau value of  $B_2^0/B_2^{(HS)} \approx (-2.7 \pm 0.2)$ . One implication of this observed scaling is that the attractive interactions that govern  $B_2^{(0)}$  are indeed roughly independent of salt concentrations above  $C_s \approx 0.25M$ . When we applied the same scaling procedure to our  $B_2$  curves, a similar plateau develops for both the DCM and the SCM models, albeit with  $B_2^{(0)}$  slightly less negative than that found in the experiments. One could, of course, very easily match to experiments by adjusting the value of  $\tau$ , but to keep contact with our earlier work [43], we don’t do so. Clearly the scaling does bring the DCM and SCM  $B_2$ ’s close together for a given  $Z$ , but for different  $Z$  (related to solution pH), the scaling collapse is not as good as that seen in experiments, since we observe a larger  $C_s$  before it sets in. Nevertheless, considering the high density of co and counter-ions in the simulation, it is remarkable that a simple Donnan theory based on ideal gas terms performs so well.

The origin of the non-monotonic variation of  $B_2^*$  with  $C_s$  can be traced back to the subtle correlation effects which cause an enhancement of the effective Coulomb repulsion



at intermediate salt concentrations in the DCM. These effects cannot be rationalized in terms of simple mean-field screening arguments [46]. The protein-microion correlations are of a different nature to those in the SCM, where they lead to a much more conventional, monotonic decay of  $B_2$  with  $C_s$ , similar to that expected from a simple screening picture.

In order to gain further insight into the physical mechanism responsible for the unusual variation of the effective Coulomb potential and of  $B_2$  with salt concentration in the DCM, we consider the influence of a second near-by protein on the microion distribution near protein-ion contact. We have computed the difference between “inner” and “outer” shell microion contact densities for  $Z = 10$ , as schematically illustrated in the inset to Figure 14. The local microion density is no longer spherically symmetric, due to the interference of the electric double-layers associated with the two proteins. The difference  $\Delta\rho = \rho_{in} - \rho_{out}$  between the mean number of microions within a fraction of a spherical shell of radius  $R = 0.6\sigma_p$  subtended by opposite  $60^\circ$  cones, is plotted in Figure 14 versus salt concentration.  $\Delta\rho$  is always positive, indicating that microions (mainly counterions) tend to cluster in the region between the proteins, rather than on the opposite sides. This follows because they can lower the total electrostatic energy by being shared between two proteins. However, there is a very significant difference in the variation of  $\Delta\rho$  with salt concentration  $C_s$ , between the SCM and the DCM models. Both exhibit similar behavior for lower salt concentrations  $C_s \leq 0.5$  Mol/l; for example, both show a small maximum around 0.2 Mol/l. But for salt concentrations above 0.5 Mol/l, the SCM predicts a monotonic decrease of  $\Delta\rho$ , while the DCM leads to a sharp peak in  $\Delta\rho$  for  $C_s \simeq 1$  Mol/l. This highly non-monotonic behavior clearly correlates with the non-monotonicity observed in Figs. 10, 11 and 12. The basic mechanism can be summarized as follows: For the DCM, the excess number of microions between the two proteins leads to an excess entropic pressure or force, as demonstrated in Figure 15, which is the origin of the increased *repulsion* between proteins around  $C_s = 1$  Mol/l. The enhanced microion density arises from subtle crowded charge correlation effects that cannot easily be understood at a mean-field level.

## V. CONCLUSION

In conclusion, we have calculated the effective interactions and the second osmotic virial coefficient  $B_2$  of protein solutions incorporating the electrostatics within the “primitive” model of electrolytes. In this way we include nonlinear screening, overscreening, and correlation effects missed within the standard Poisson-Boltzmann description. For discrete charge distributions, the interactions and related  $B_2$  vary in a non-monotonic fashion for increasing ion strength while for the smeared charge model, a standard workhorse of colloidal physics, this effect is absent. These correlation induced effects are missed within non-linear PB theory, and similar coarse-graining techniques taken from the theory of colloids. In addition to this, our simulations indicate *the necessity of taking entropic forces into account* when treating systems on the nanoscale. These forces are believed to be essential in the salting-out effect [62] and could lead to an attraction even between neutral globular proteins [24].

Our MD calculations can easily be extended to the more complex (pH dependent) charge patterns of realistic proteins [72]. In fact, in some cases it may be easier to do a full MD simulation than to solve the non-linear PB equations in a very complicated geometry. We expect similar mechanisms to those found for the DCM to be active there, leading, for example, to an enhanced protein-protein repulsion at intermediate salt concentration. Since the second osmotic virial coefficient determines much of the excess (non-ideal) part of the chemical potential of semi-dilute protein solutions, we expect the non-monotonicity of  $B_2$  to have a significant influence on protein crystallization from such solutions in the course of a “salting-out” process. The non-monotonic behavior also suggests the possibility of an inverse, “salting-in” effect, whereby a reduction of salt concentration may bring  $B_2$  into the “crystallization slot” [3,12]. The sensitivity of  $B_2$  to ion-correlation effects may help explain the salt specificity of the Hofmeister series [62]. Finally, we stress that our non-monotonicity is qualitatively different from that observed for added non-adsorbing [73,74] and absorbing [75] polymers.

## ACKNOWLEDGMENTS

The authors are grateful to R. Piazza, I.L. Alberts, P.G. Bolhuis, G. Bricogne, J. Clarke, S. Egelhaaf, J.F. Joanny, D. Rowan, R. Blaak and W.C.K. Poon for useful discussions, and to Schlumberger Cambridge Research and the Isaac Newton Trust for financial support.

## REFERENCES

- [1] S. D. Durbin, G. Feher, *Annu. Rev. Phys. Chem.* **47**, 171 (1996).
- [2] A. Tardieu, A. Le Verge, M. Malfois, F. Bonneté, S. Finet, M. Riés-Kautt, L. Belloni, *J. Crystal Growth* **196**, 193 (1999).
- [3] A. George, W. Wilson, *Acta Crystallogr. D* **50**, 361 (1994); A. George, Y. Chiang, B. Guo, A. Arabshahi, Z. Cai, W. W. Wilson, *Methods Enzymol* **276**, 100 (1997).
- [4] F. Rosenberger, P. G. Vekilov, M. Muschol, B. R. Thomas, *Journal of Crystal Growth* **168**, 1 (1996).
- [5] R. Piazza, *Current Opinion in Colloid and Interface Science* **5**, 38 (2000).
- [6] K. A. Dill, *Nature* **400**, 309 (1999).
- [7] S. Tamashima, *Biopolymers* **58**, 398 (2001).
- [8] B. V. Derjaguin, L. D. Landau, *Acta Physicochim. USSR* **14**, 633 (1941); E. J. W. Verwey and J. T. G. Overbeek, "Theory of the Stability of Lyophobic Colloids" (Elsevier, Amsterdam, 1948).
- [9] G. M. Kepler, S. Fraden, *Phys. Rev. Lett.* **73**, 356 (1994).
- [10] A. E. Larson, *Nature* **385**, 230 (1997).
- [11] R. Verma, J. C. Crocker, T. C. Lubensky, A. G. Yodh, *Phys. Rev. Lett.* **81**, 4004 (1998).
- [12] D. F. Rosenbaum, C. F. Zukoski, *J. Cryst. Growth* **169**, 752 (1996).
- [13] Y. U. Moon, R. A. Curtis, C. O. Anderson, H. W. Blanch, J. M. Prausnitz, *Journal of Solution Chemistry* **29**, 699 (2000).
- [14] Y. U. Moon, C. O. Anderson, H. W. Blanch, J. M. Prausnitz, *Fluid Phase Equilibria* **168**, 229 (2000).
- [15] D. Rosenbaum, P. C. Zamora, C. F. Zukoski, *Phys. Rev. Lett.* **76**, 150 (1995).

- [16] G. A. Vliegenthart, H. N. W. Lekkerkerker, J. Chem. Phys. **112**, 5364 (2000).
- [17] M. H. J. Hagen, D. Frenkel, J. Chem. Phys. **101**, 4093 (1994).
- [18] M. Muschol, F. Rosenberger, J. Chem. Phys. **107**, 1953 (1997).
- [19] M. Malfois, F. Bonneté, L. Belloni, A. Tardieu, J. Chem. Phys. **105**, 3290 (1996).
- [20] P. R. ten Wolde, D. Frenkel, Theoretical Chemistry Accounts **101**, 205 (1999).
- [21] P. M. Tessier, A. M. Lenhoff, S. I. Sandler, Biophysical Journal **82**, 1620 (2002).
- [22] N. Sun, J. Y. Walz, Journal of Colloid and Interface Science **234**, 90 (2001).
- [23] D. F. Rosenbaum, A. Kulkarni, S. Ramakrishnan, C. F. Zukoski, J. Chem. Phys. **111**, 9882 (1999).
- [24] J. Wu, D. Bratko, H. W. Blanch, J. M. Prausnitz, J. Chem. Phys. **111**, 7084 (1999); J. Z. Wu, D. Bratko, H. W. Blanch, J. M. Prausnitz, Phys. Rev. E **62**, 5273 (2000).
- [25] M. L. Broide, T. M. Tominc, M. D. Saxowsky, Phys. Rev. E **53**, 6325 (1996).
- [26] V. G. Taratuta, A. Holschbach, G. M. Thurston, D. Blankschtein, G. B. Benedek, J. Phys. Chem. **94**, 2140 (1990).
- [27] T. Arakawa, R. Bhat, S. N. Timasheff, Biochemistry **29**, 1914 (1990).
- [28] C. Haas, J. Drenth, W. W. Wilson, J. Phys. Chem. B **103**, 2808 (1999).
- [29] J. J. Grigsby, H. W. Blanch, J. M. Prausnitz, J. Phys. Chem. B **104**, 3645 (2000).
- [30] B. Guo, S. Kao, H. McDonald, A. Asanov, L. L. Combs, W. W. Wilson, J. Crystal Growth **196**, 424 (1999).
- [31] F. Bonneté, S. Finet, A. Tardieu, J. Crystal Growth **196**, 403 (1999).
- [32] R. Piazza, J. Crystal Growth **196**, 415 (1999).
- [33] R. J. Baxter, J. Chem. Phys. **49**, 2770 (1968).

- [34] W. C. K. Poon, Phys. Rev. E **55**, 3762 (1997).
- [35] W. C. K. Poon, S. U. Egelhaaf, P. A. Beales, A. Salonen, L. Sawyer, J. Phys. Condensed Matter **12**, L569 (2000).
- [36] B. L. Neal, D. Asthagiri, A. M. Lenhoff, Biophysical Journal **75**, 2469 (1998); B. L. Neal, D. Asthagiri, O. D. Velev, A. M. Lenhoff, E. W. Kaler, J. Crystal Growth **196**, 377 (1999).
- [37] R. P. Sear, J. Chem. Phys. **111**, 4800 (1999).
- [38] A. Lomakin, N. Asherie, G. B. Benedek, Proc. Natl. Acad. Science, USA **96**, 9465 (1999).
- [39] E. Allahyarov, I. D’Amico, H. Löwen, Phys. Rev. Lett. **81**, 1334 (1998).
- [40] P. Linse, V. Lobaskin, Phys. Rev. Lett. **83**, 4208 (1999); J. Chem. Phys. **112**, 3917 (2000).
- [41] N. Grønbech-Jensen, K. M. Beardmore, P. Pincus, Physica A **261**, 74 (1998).
- [42] J. P. Hansen, H. Löwen, Annual Rev. Phys. Chem. **51**, 209 (2000).
- [43] E. Allahyarov, H. Löwen, J. P. Hansen, A. A. Louis, Europhys. Letters. **57**, 731 (2002).
- [44] H. L. Friedman, "Ionic Solution Theory" (Wiley Interscience, New York, 1962).
- [45] F. Carlsson, P. Linse, M. Malmsten, J. Phys. Chem. B **105**, 9040 (2001).
- [46] F. Carlsson, M. Malmsten, P. Linse, J. Phys. Chem. B **105**, 12189 (2001).
- [47] T. Erber, G. M. Hockney, Advances in Chem. Phys., **98**, 495 (1997).
- [48] E. Allahyarov, H. Löwen, S. Trigger, Phys. Rev. E **57**, 5818 (1998).
- [49] E. Allahyarov, H. Löwen, Phys. Rev. E **62**, 5542 (2000).
- [50] P. Attard, J. Chem. Phys. **91**, 3083 (1989).

- [51] J. Piasecki, L. Bocquet, J. P. Hansen, *Physica A* **218**, 125 (1995).
- [52] J. Lekner, *Physica A* **176**, 485 (1991); J. Lekner, *Mol. Simul.* **20**, 357 (1998).
- [53] C. Tanford, R. Roxby, *Biochemistry* **11**, 2192 (1972).
- [54] D. R. Berard, P. Attard, G. N. Patey, *J. Chem. Phys.* **98**, 7236 (1993).
- [55] A. A. Louis, E. Allahyarov, H. Löwen, R. Roth, to appear in *Phys. Rev. E.* (2002).
- [56] R. R. Netz, *Phys. Rev. Letters* **60**, 3174 (1999).
- [57] P. C. Zamora, C. F. Zukoski, *Langmuir* **12**, 3541 (1996).
- [58] S. B. Howard, P. J. Twigg, J. K. Baird, E. J. Meehan, *J. Cryst. Growth* **90**, 94 (1988).
- [59] F. Rosenberger, S. B. Howard, J. W. Sowers, T. A. Nyce, *J. Cryst. Growth* **129**, 1 (1993)
- [60] E. Cacioppo, M. L. Pusey, *J. Cryst. Growth* **144**, 286 (1991).
- [61] R. Messina, C. Holm, K. Kremer, *Phys. Rev. Lett.* **85**, 872 (2000).
- [62] R. Piazza, M. Pierno, *J. Phys. Condensed Matter* **12**, A443 (2000).
- [63] V. Vlachy, H. W. Blanch, J. M. Prausnitz, *AIChE J.* **39**, 215 (1993).
- [64] C. J. Coen, H. W. Blanch, J. M. Prausnitz, *AIChE J.* **41**, 996 (1995).
- [65] D. Stigter, *Biopolymers* **46**, 503 (1998).
- [66] J. J. Delrow, J. A. Gebe, J. M. Schurr, *Biopolymers* **42**, 455 (1997).
- [67] C. Vega, P. A. Monson, *J. Chem. Phys.* **109**, 9938 (1998).
- [68] C. O. Anderson, J. F. M. Niesen, H. W. Blanch, J. M. Prausnitz, *Biophysical Chemistry* **84**, 177 (2000).
- [69] R. Piazza, V. Peyre, V. Degiorgio, *Phys. Rev. E* **58**, R2733 (1998).

- [70] A. A. Louis, Phil. Trans. Roy. Soc. A **359**, 939 (2001)
- [71] P. B. Warren, preprint, cond-mat/0201418
- [72] M. Boyer, M.-O. Roy, M. Jullien, F. Bonnetè, A. Tardieu, J. Cryst. Growth **196**, 185 (1999).
- [73] A. M. Kulkarni, A. P. Chatterjee, K. S. Schweizer, C. F. Zukoski, Phys. Rev. Lett. **83**, 4554 (1999).
- [74] E. Eisenriegler, J. Chem. Phys. **113**, 5091 (2000).
- [75] L. V. Zherenkova, D. A. Mologin, P. G. Khalatur, A. R. Khokhlov, Colloid and Polymer Sci. **276**, 753 (1998).



# TABLES

TABLE I. Parameters used for the different simulation runs.  $N_s$  is the number of salt ion pairs in simulation box,  $C_s$  is the salt concentration in Mol/l, the Debye screening length  $r_D$  is defined by Eqn.(10) and  $r_s = \left( \frac{3V'}{4\pi(2N_s+2Z)} \right)^{\frac{1}{3}}$  is the average distance between salt ions for a given salt concentration.

Run	$N_s$	$C_s$ (Mol/l)	$r_D/\sigma_p$	$r_s/\sigma_p$
1	0	0	0	0
2	125	0.05	0.34	0.39
3	250	0.103	0.24	0.31
4	500	0.206	0.17	0.25
5	1000	0.412	0.12	0.2
6	1500	0.62	0.1	0.17
7	2000	0.824	0.085	0.16
8	2500	1.03	0.077	0.15
9	3000	1.24	0.07	0.14
10	4000	1.65	0.06	0.124
11	5000	2.061	0.054	0.118

# FIGURES

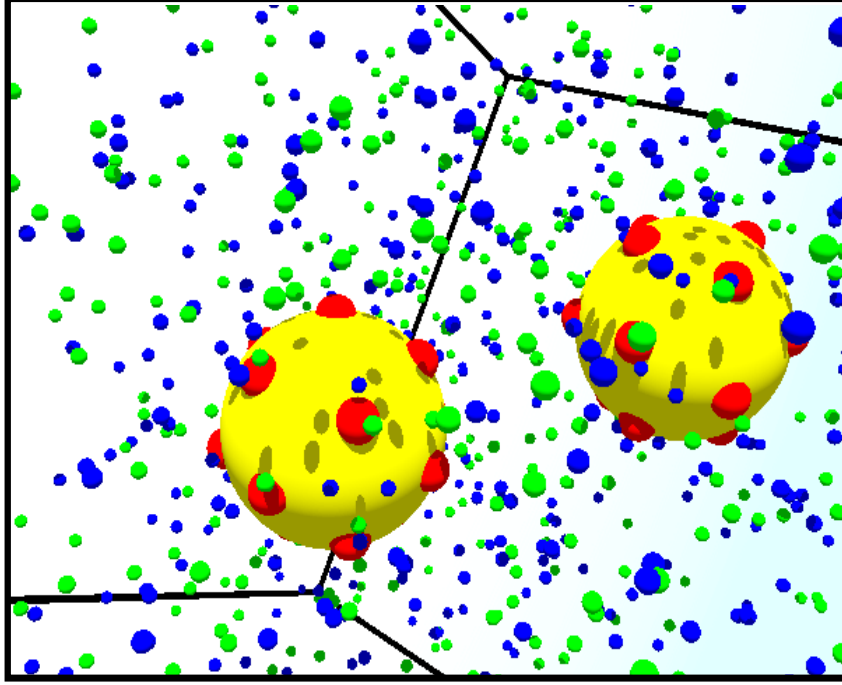


FIG. 1. Snapshot of a typical MD-generated microion configuration around two proteins, separated by  $r = 1.7\sigma_p$ . The proteins carry 15 discrete charges  $-e$  and the monovalent salt density is  $C_s = 0.206$  Mol/l. The globular protein molecules are shown as two large gray spheres. The embedded small dark spheres on their surface mimic the discrete protein charges in the DCM model. The small gray spheres are counterions, while the black spheres are coions.

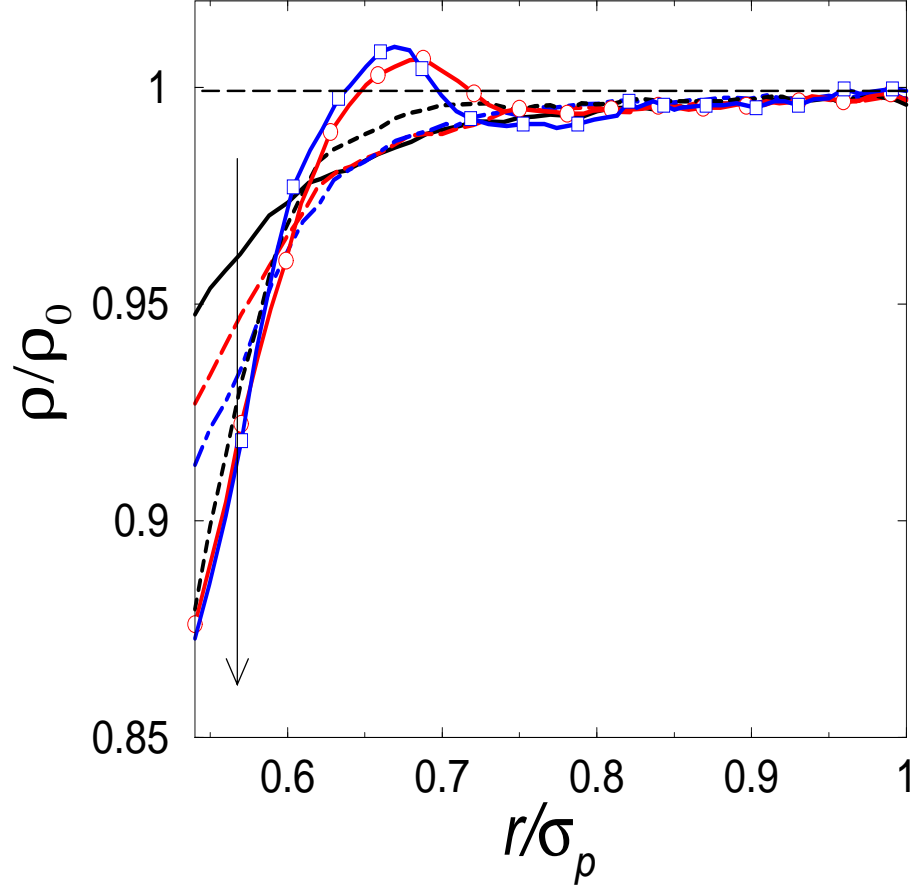


FIG. 2. Normalized total salt density profiles  $\rho(r)$  near single *neutral sphere*.  $\rho_0 = N_s/V'$  is bulk density. The added salt concentration is increased from top to bottom (see the arrow which refers to the  $\rho(r)$  near protein surface) according to runs 1-5, 7, 9.

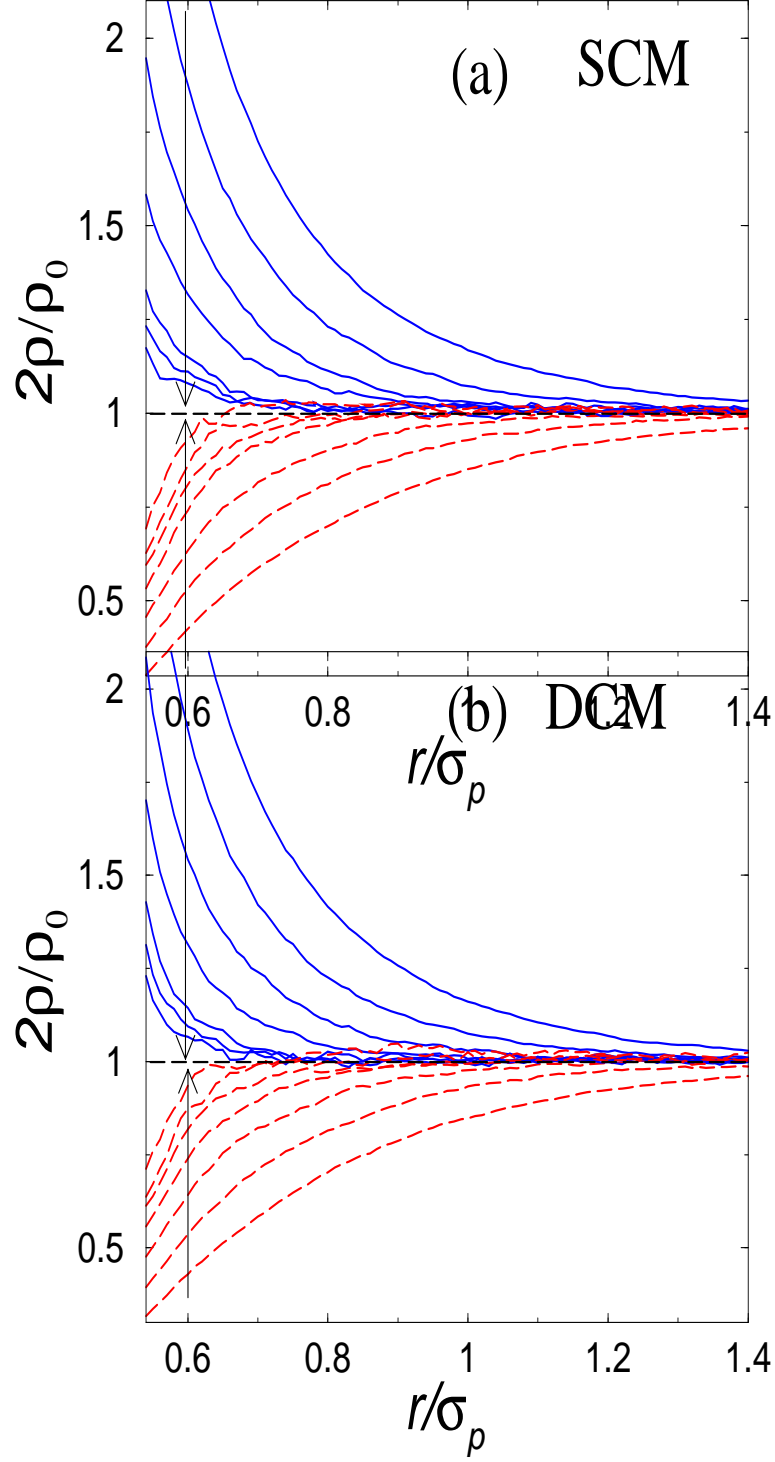


FIG. 3. Rescaled density profiles of small ions near single protein surface for the SCM (a) and DCM (b) models. The protein charge is  $Z = 10$ . The added salt concentration is increased (shown by an arrow) from top to bottom for solid lines (counterions) and from bottom to top for dashed lines (coions), according to runs 2-5, 7, 9, 11.

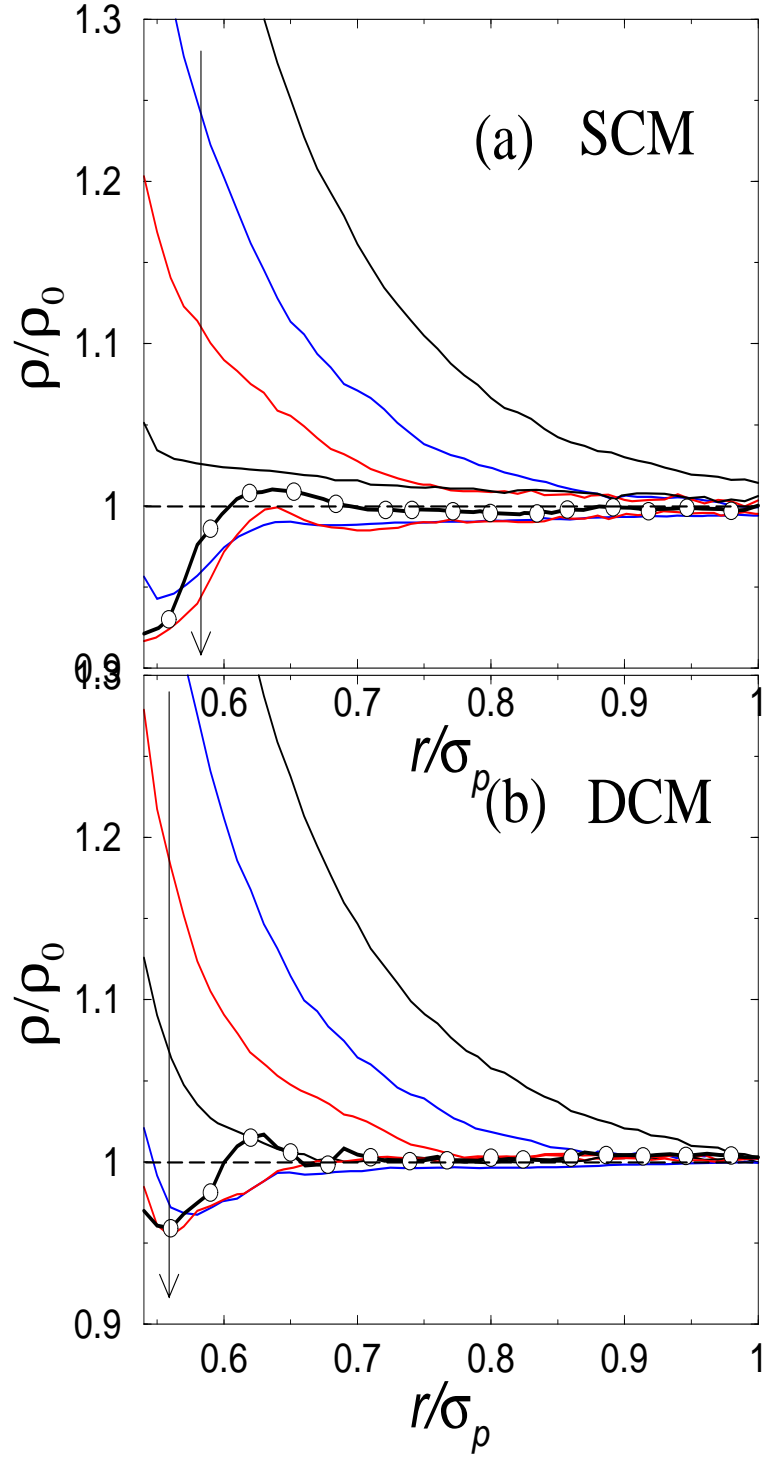


FIG. 4. Same runs as Figure 3, but now for the total salt density near single protein surface. The arrow (a direction of added salt increase) applies to all runs except run 11, which is shown as a solid line with symbols.

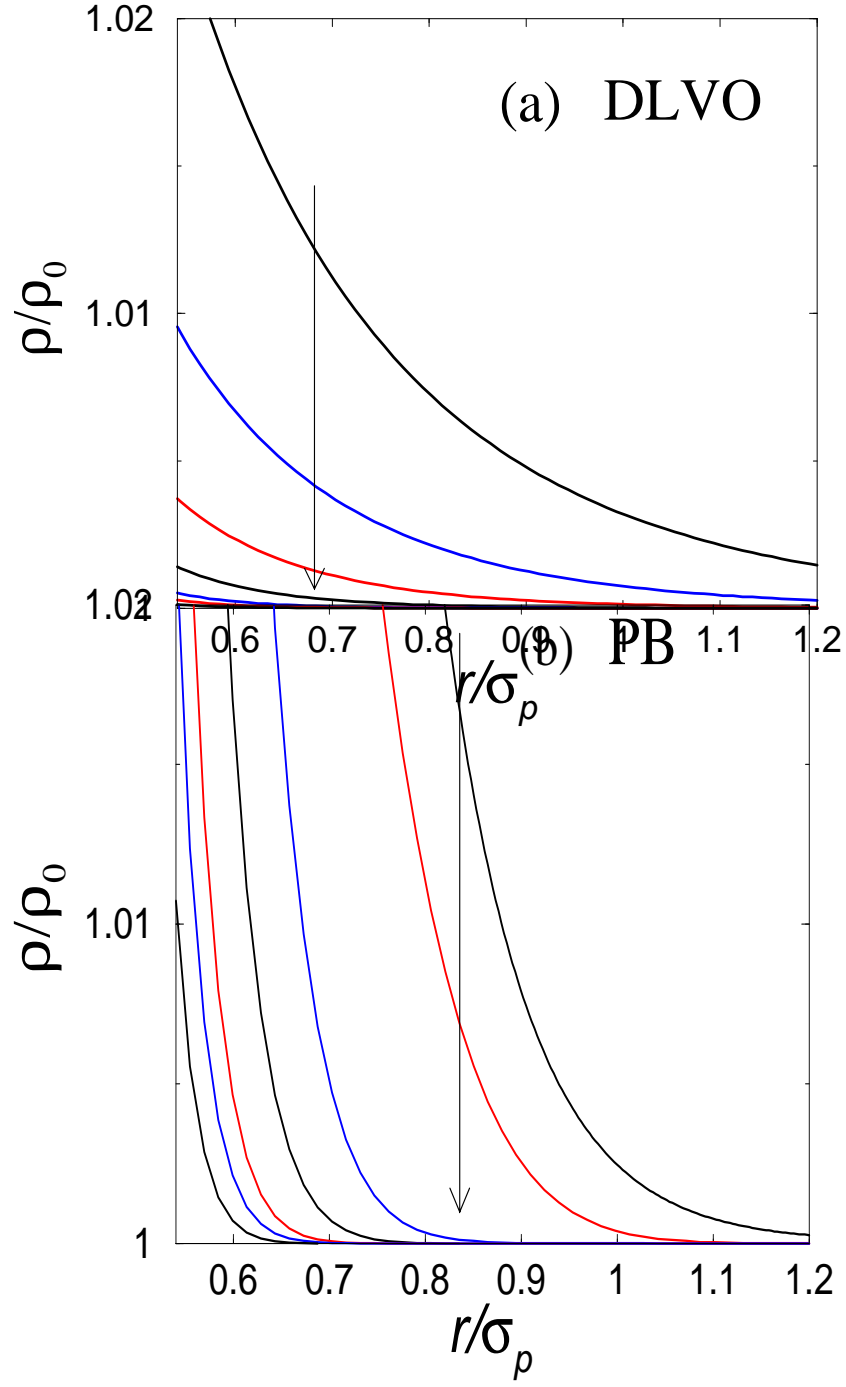


FIG. 5. Same runs as in Figure 4, but now for DLVO theory (a), and non-linear PB theory (b); both are for the SCM.

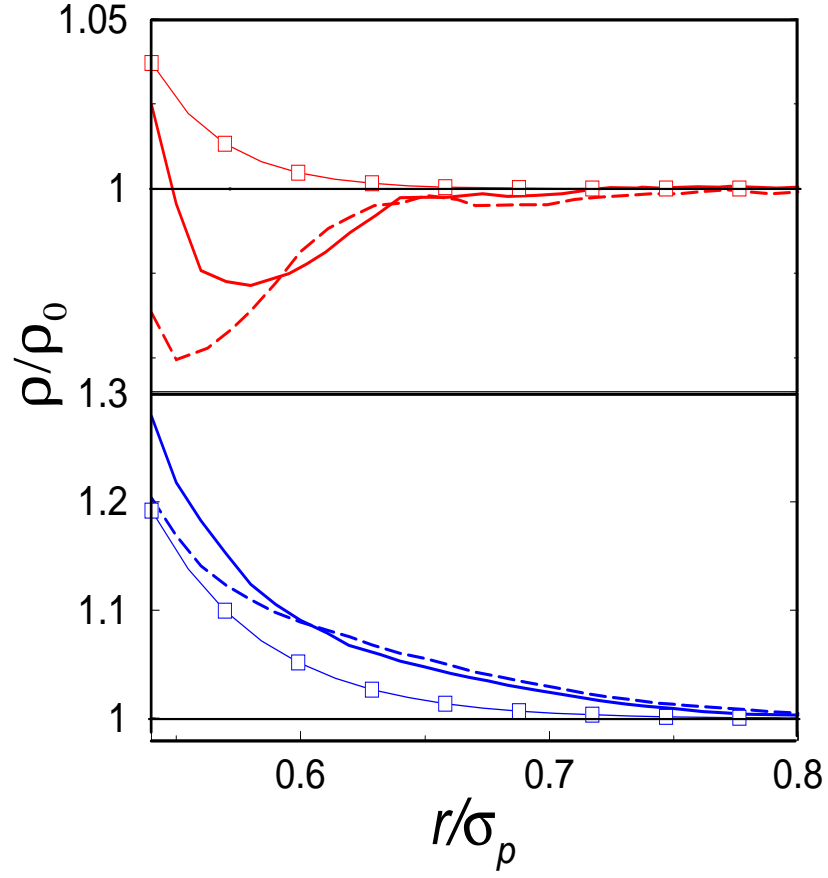


FIG. 6. Total density profiles  $\rho(r)$  of salt ions around a single protein with  $Z = 10$ , for run 4 (bottom set of curves) and run 7 (upper set of curves), comparing DCM simulations (solid line), SCM simulations (dashed line), and nonlinear Poisson-Boltzmann theory (squares connected by lines).

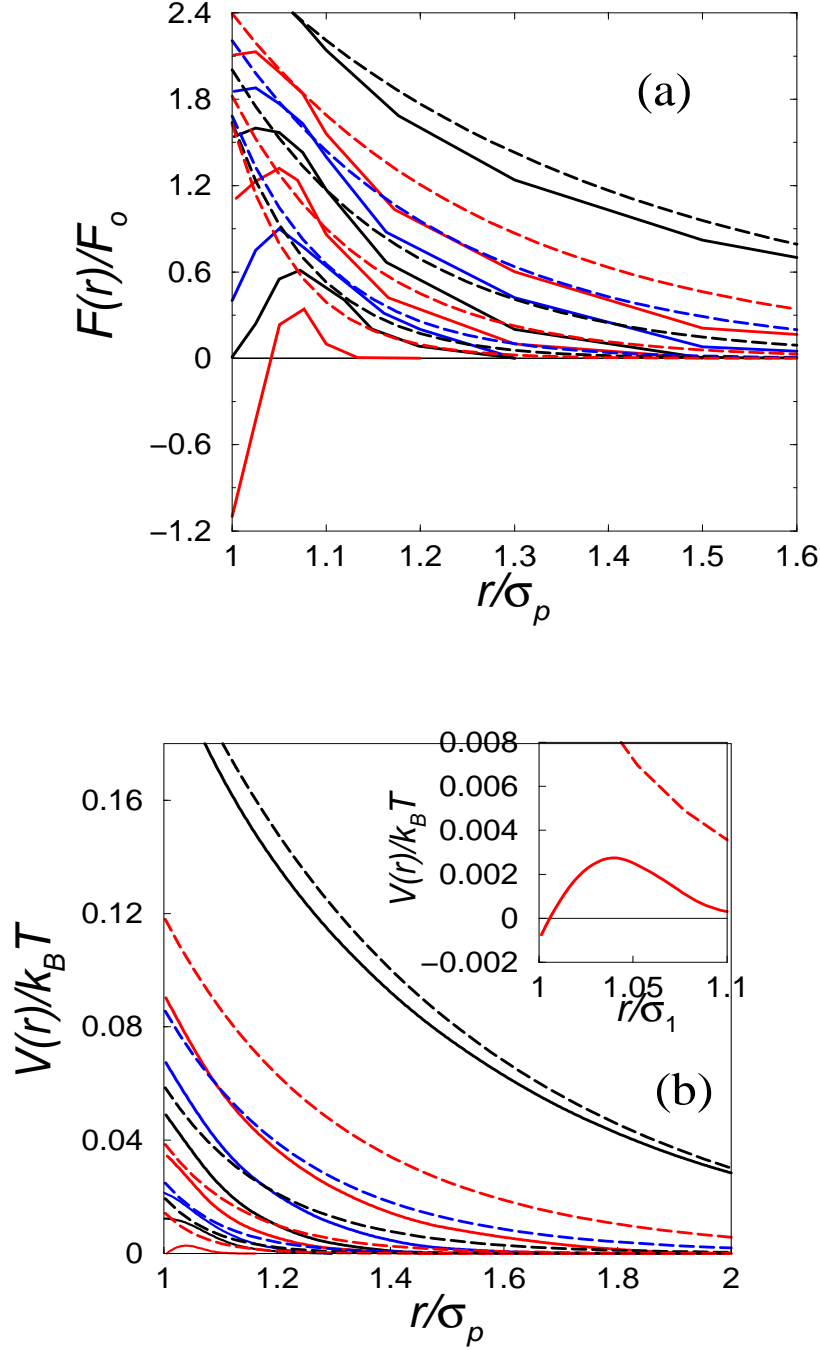


FIG. 7. Total interaction force  $F(r)$  (a) and interaction potential  $V(r)$  (b) versus dimensionless separation distance  $r/\sigma_p$  within the SCM for a protein charge  $Z = 10$ . The force is divided by  $F_0 = k_B T / \lambda_B$ , where  $\lambda_B = e^2 / \epsilon k_B T$  is the Bjerrum length. The added salt concentration is increased from top to bottom, according to runs 1-5, 7, 9, 11. Dashed lines correspond to the DLVO model. The inset in (b) shows in more detail the differences between the SCM simulations and the DLVO model potential for run 11.



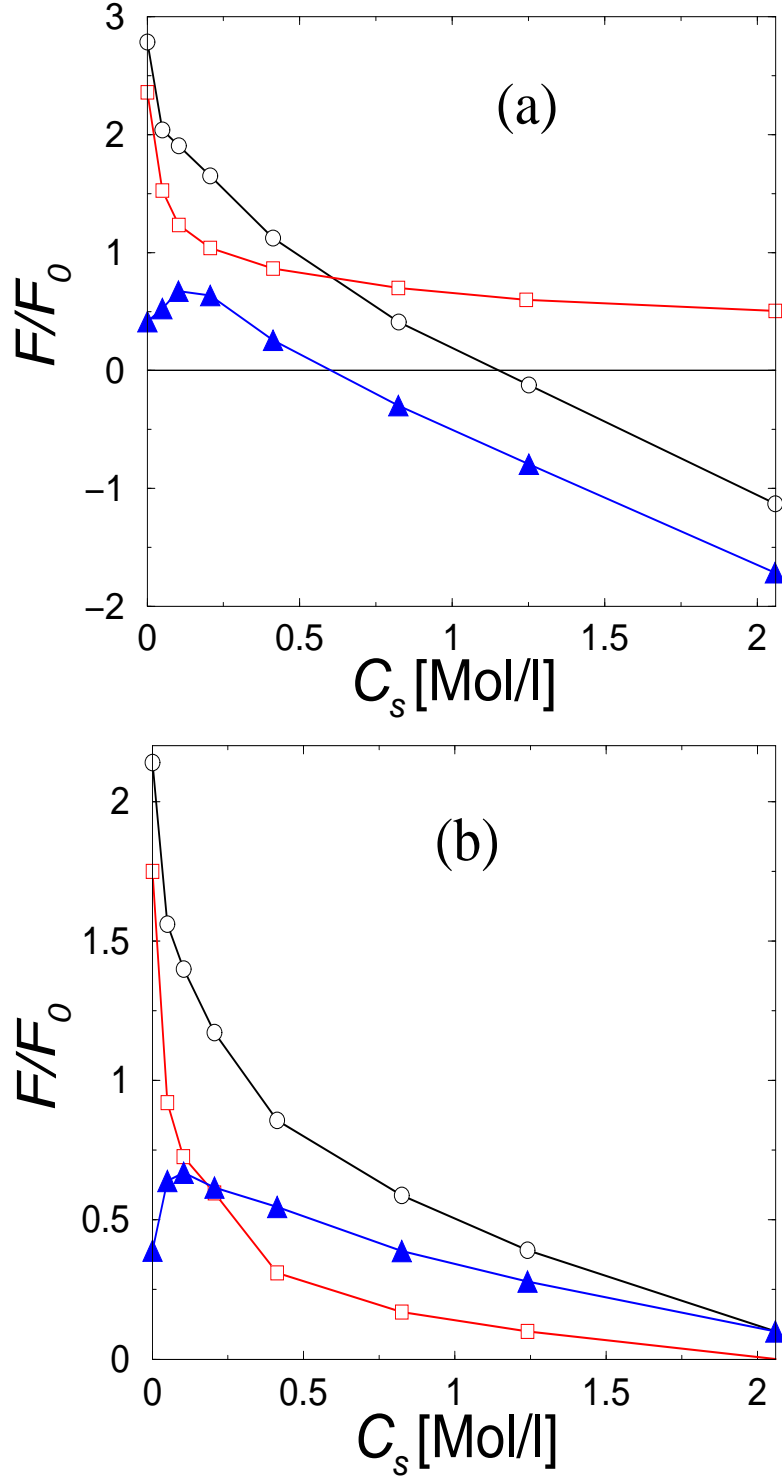


FIG. 8. The total interaction force  $F$  (circles) and its electrostatic,  $F^{(2)}$  (squares) and entropic  $F^{(3)}$  (triangles) components versus salt concentration. The separation distance is fixed at (a)  $r/\sigma_p = 1$  and (b)  $r/\sigma_p = 1.1$ . The simulations are for the SCM with  $Z = 10$ , and show that at high salt concentrations, the entropic force dominates.

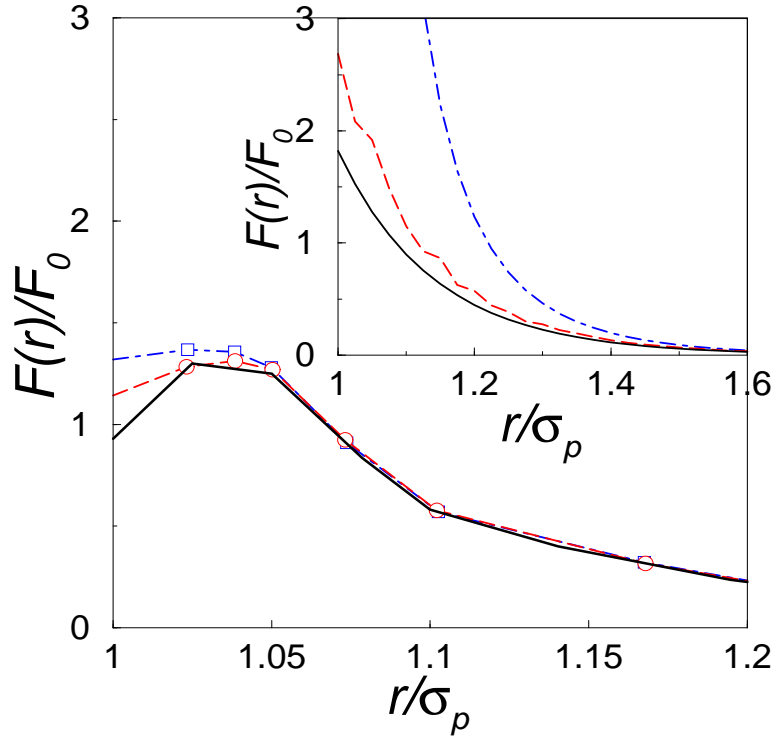
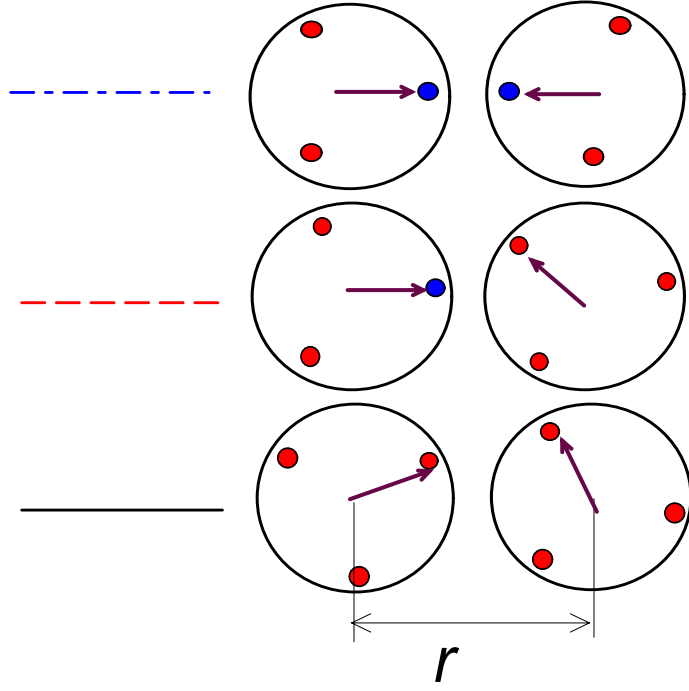


FIG. 9. (a) An illustration of three different mutual orientations of two proteins. Points inside spheres represent protein charges in the DCM. (b) Total interaction force  $F(r)$  versus dimensionless separation distance  $r/\sigma_p$  for mutual orientations shown in (a) for run 5 and  $Z = 10$  in the DCM. The inset shows the same, but for a Yukawa segment model.

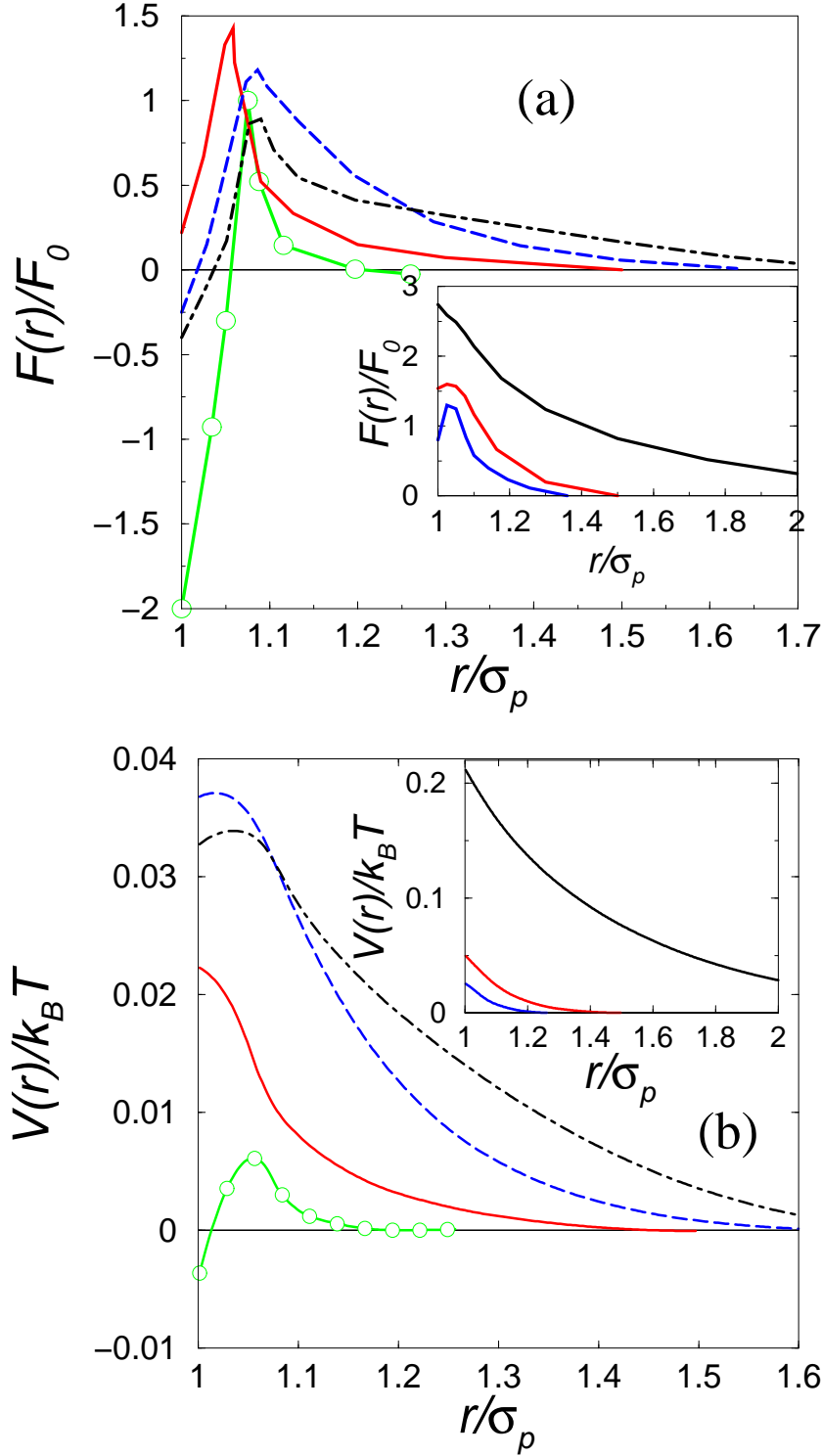


FIG. 10. Total interaction force  $F(r)$  (a) and interaction potential  $V(r)$  (b) versus dimensionless separation distance  $r/\sigma_p$  for the DCM at  $Z = 10$ . Solid line- run 7, dashed line- run 8, dot-dashed line- run 9, open circles- run 11. The inset shows low salt concentrations, from top to bottom: runs 1, 4, 5.

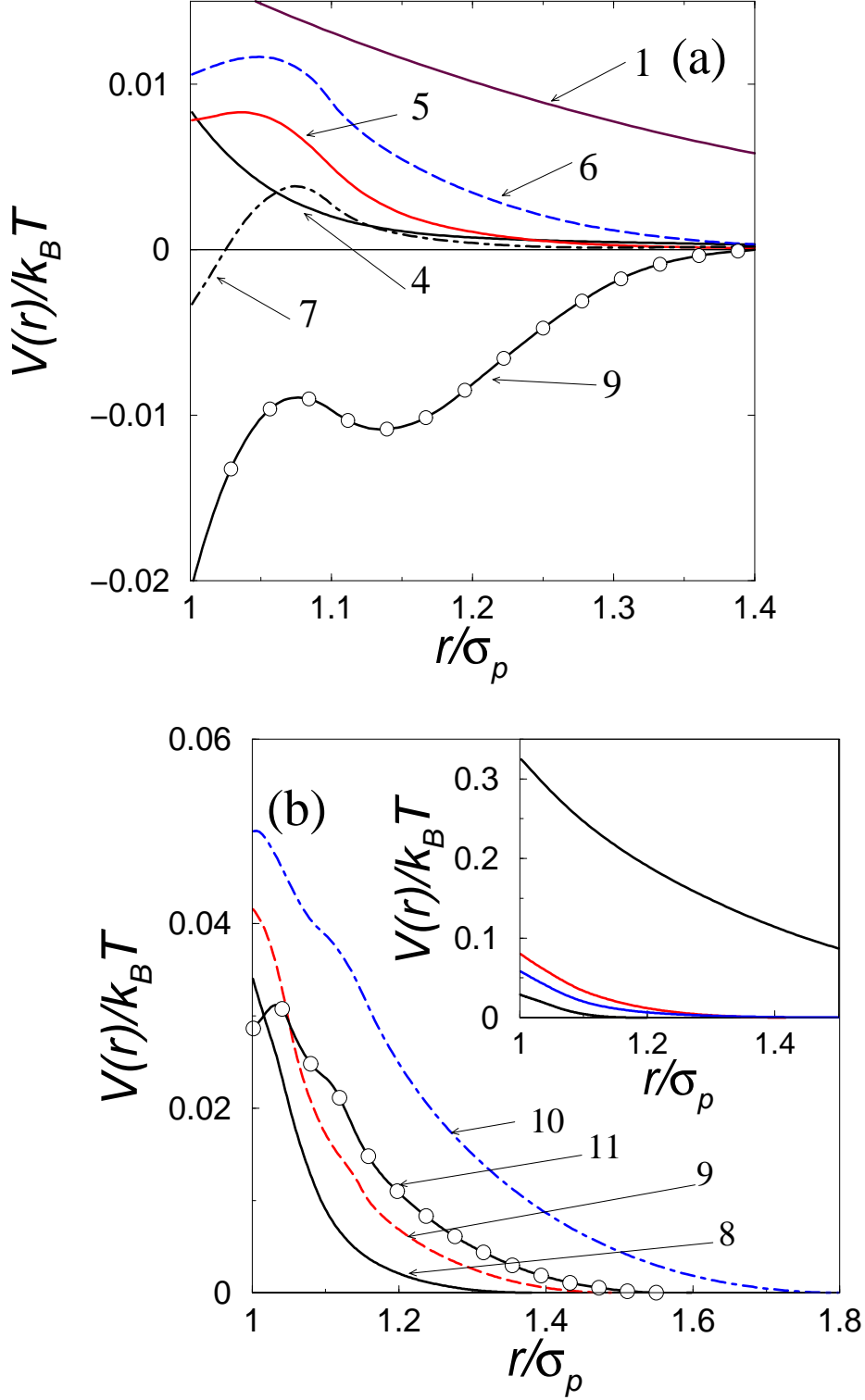


FIG. 11. The same as in Figure 10 but now for protein charge (a)  $Z = 6$  and (b)  $Z = 15$ . The run numbers are placed next to corresponding curves. The result for run 1 is 4 times reduced in  $y$ -value to fit the  $y$ -axis scale. The inset in (b) shows low salt concentrations, from top to bottom, runs 1, 4, 5, 7.

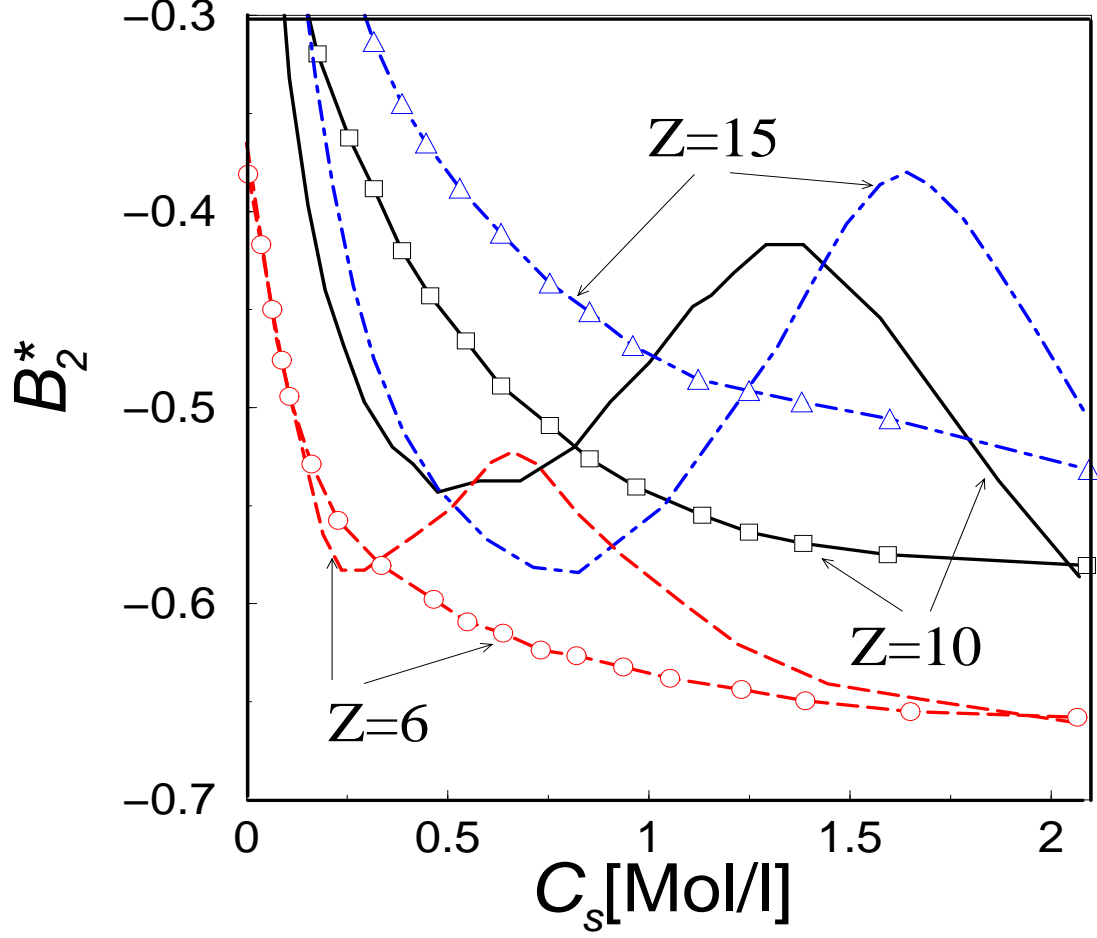


FIG. 12. Normalized second virial coefficient  $B_2^* = B_2/B_2^{HS}$  of a protein solution versus salt concentration  $C_s$ . Results are shown for protein charges  $Z = 6$  (dashed lines),  $Z = 10$  (solid lines) and  $Z = 15$  (dot-dashed lines). The lines with (without) symbols correspond to the SCM (DCM) model. Whereas the SCM virial coefficients decrease monotonically with increasing salt concentration, as expected from simple screening arguments, the DCM shows a marked *nonmonotonic* increase of  $B_2$  at intermediate salt concentrations.

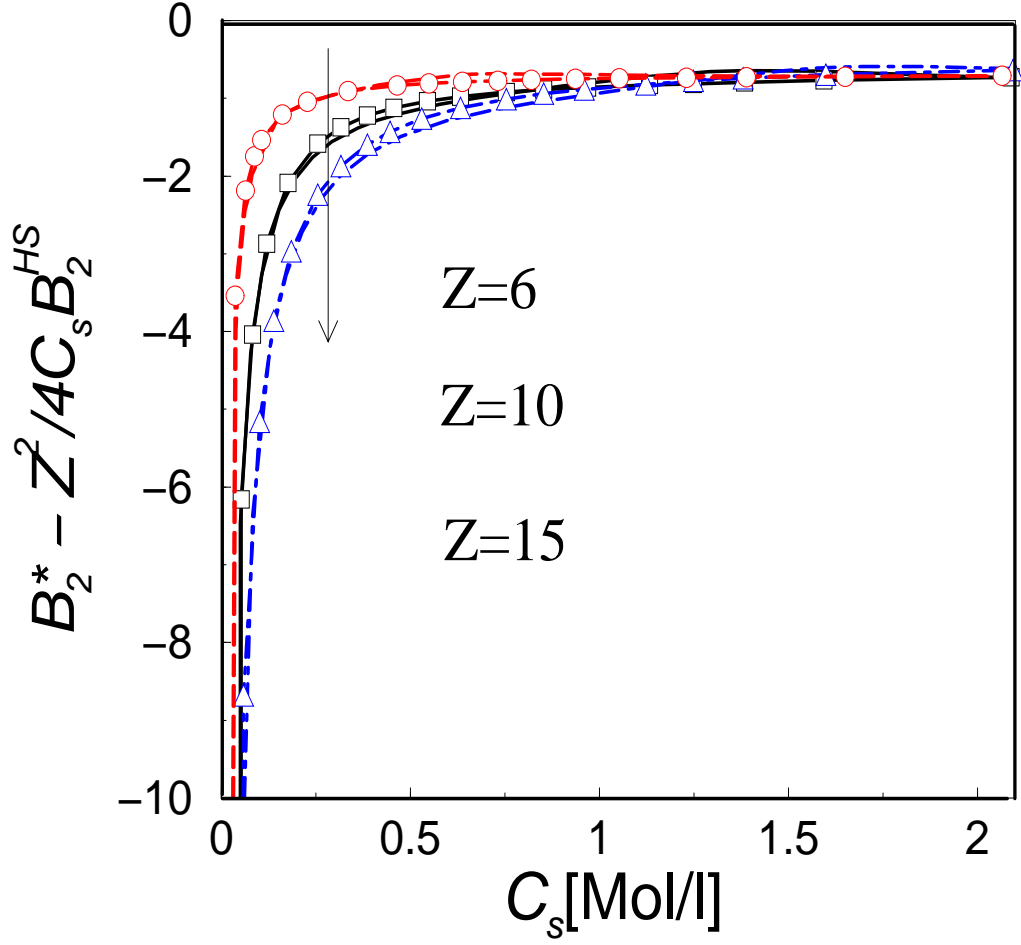


FIG. 13. The same runs as in Figure 12, but now for the bare virial coefficient determined as  $\frac{B_2 - Z^2/4C_s}{B_2^{(HS)}}$ . The arrow is a guide for eye for the direction of increasing protein charge  $Z$ . The scaling collapse at high  $C_s$  has been related to a Donnan equilibrium effect [71]. Note that, on the scale shown, the nonmonotonicity is hardly visible.

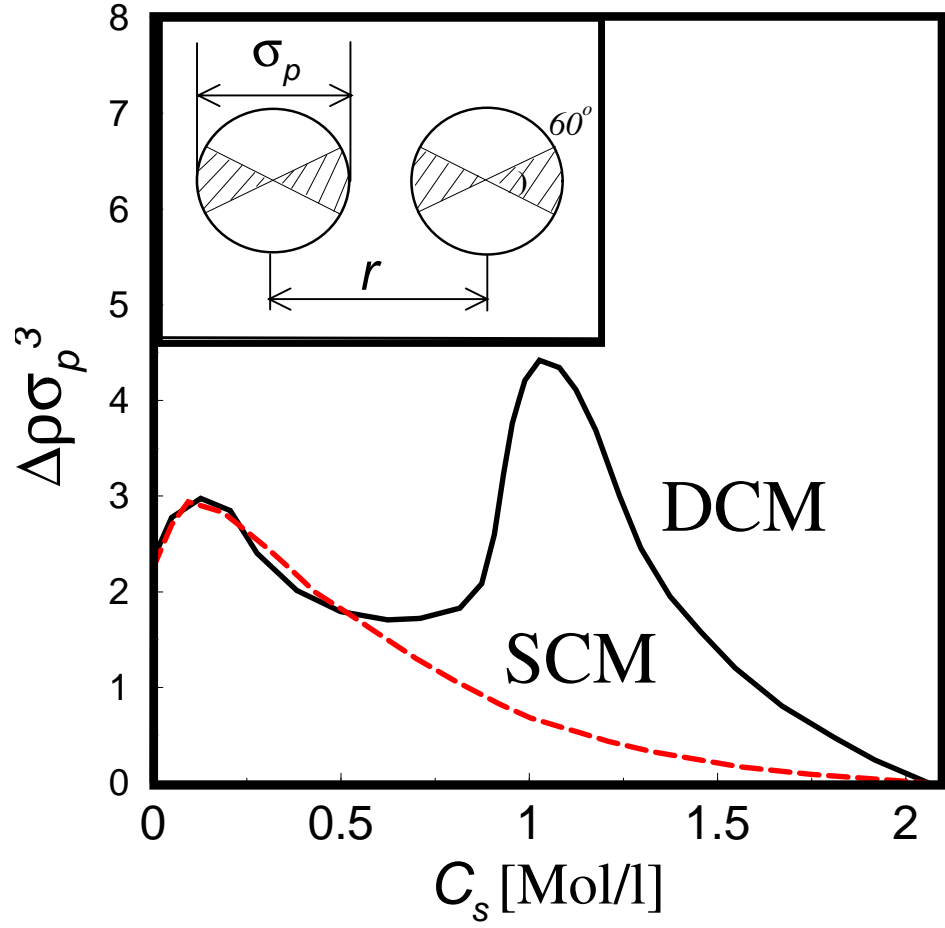


FIG. 14. Difference in the microion density near contact  $\Delta\rho$  versus salt concentration for protein charge  $Z = 10$  at a protein-protein separation of  $r = 1.2\sigma_p$ . The solid and dashed lines correspond to the DCM and SCM models respectively. The inset shows the angular range over which  $\Delta\rho$  is averaged (see text). The non-monotonic density profile for the DCM lies at the origin of the non-monotonic behavior seen for the forces, potentials, and virial coefficients calculated for this model.

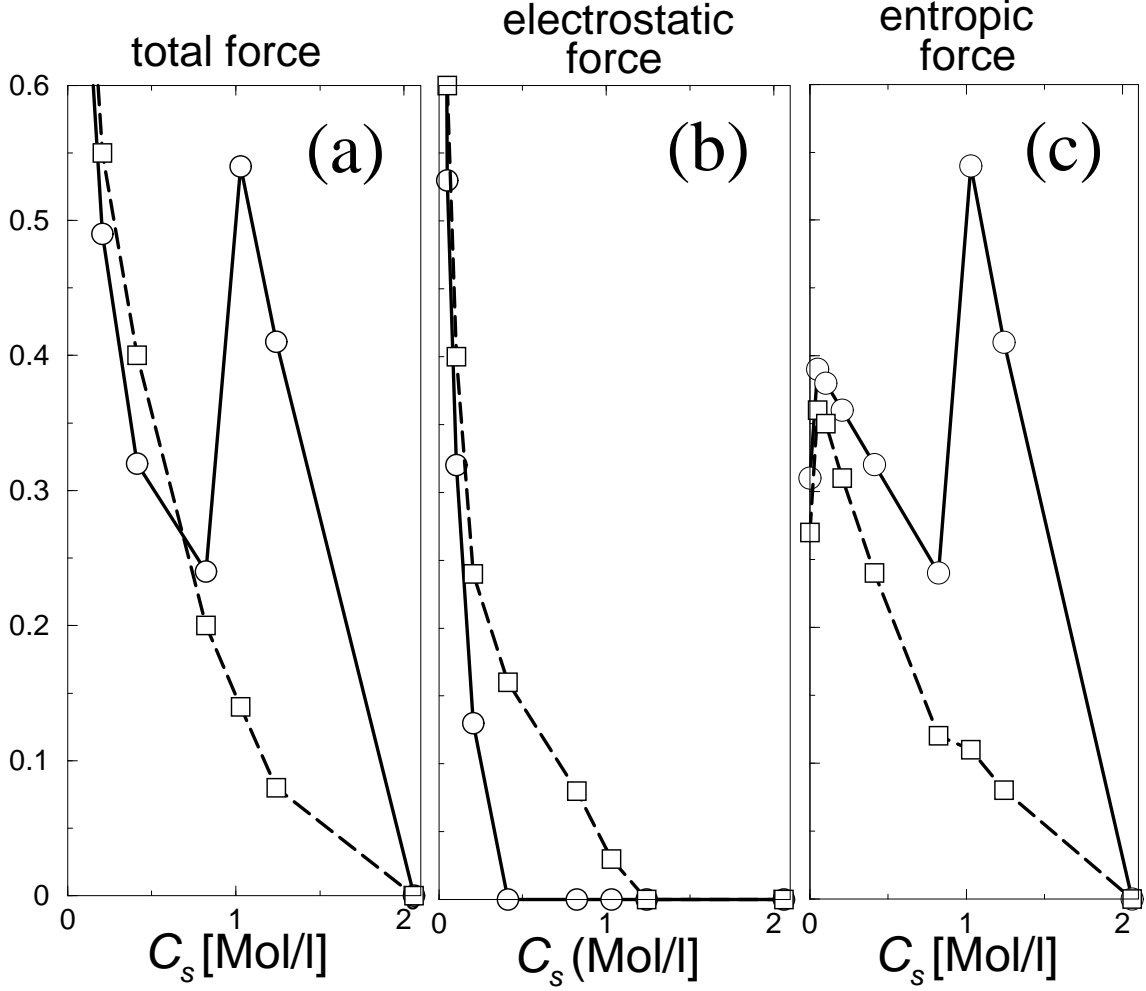


FIG. 15. The protein-protein interaction force and its components at a protein-protein separation  $r = 1.2\sigma_p$ , in units of  $k_B T / \lambda_B$ , versus salt concentration  $C_s$  for a charge of  $Z = 10$ . From left to right: (a)- total interaction force, (b)- electrostatic component of interaction force, (c)- entropic component of interaction force. Solid line- DCM and dashed line- SCM results. This figure demonstrates that the difference between the two models arises primarily from the contributions of the entropic force.



## APPENDIX A: MULTIPOLE EXPANSION OF COUNTERION DENSITY AROUND PROTEIN IN DCM

We expand the numerically calculated counterion density around a protein with charge  $Z$  in a Laplace series of spherical harmonics:

$$\rho(r, \theta, \varphi) = \sum_{n,m} C_{nm}(r) P_n^m(\cos(\theta)) \cos(m\varphi) + S_{nm}(r) P_n^m(\cos(\theta)) \sin(m\varphi) \quad (\text{A1})$$

The multipole spherical expansion coefficients (MSEC) are calculated during an MD simulation via

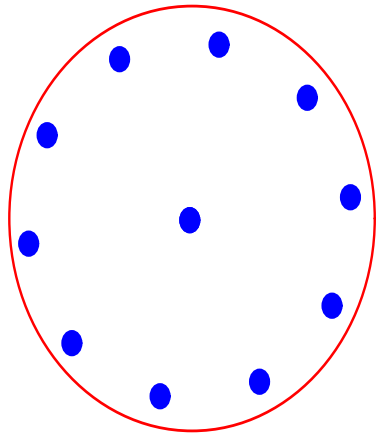
$$\begin{aligned} C_{00} &= \langle \sum_i \delta(\vec{r} - \vec{r}_i) \rangle, \\ C_{10} &= \langle \sum_i \delta(\vec{r} - \vec{r}_i) \cos(\theta_i) \rangle, \\ C_{11} &= \langle \sum_i \delta(\vec{r} - \vec{r}_i) \sin(\theta_i) \cos(\varphi_i) \rangle, \\ S_{11} &= \langle \sum_i \delta(\vec{r} - \vec{r}_i) \sin(\theta_i) \sin(\varphi_i) \rangle, \\ C_{20} &= \langle \sum_i \delta(\vec{r} - \vec{r}_i) \frac{3 \cos^2(\theta_i) - 1}{2} \rangle, \\ C_{21} &= \langle \sum_i \delta(\vec{r} - \vec{r}_i) 3 \sin(\theta_i) \cos(\theta_i) \cos(\varphi_i) \rangle, \\ S_{21} &= \langle \sum_i \delta(\vec{r} - \vec{r}_i) 3 \sin(\theta_i) \cos(\theta_i) \sin(\varphi_i) \rangle, \\ C_{22} &= \langle \sum_i \delta(\vec{r} - \vec{r}_i) 3 \sin^2(\theta_i) \cos(2\varphi_i) \rangle, \\ S_{22} &= \langle \sum_i \delta(\vec{r} - \vec{r}_i) 3 \sin^2(\theta_i) \sin(2\varphi_i) \rangle, \end{aligned}$$

where  $i$  runs over counterions.

The protein charge is chosen to be  $Z = 12$ , so that the rotation symmetry axis through two surface charges has a fivefold symmetry. The  $xz$  and  $xy$  plane projections of the protein charge pattern are shown in Figure 16.

The variation of the nonzero MSEC versus distance from the protein center are shown in Figure 17.

(a)



(b)

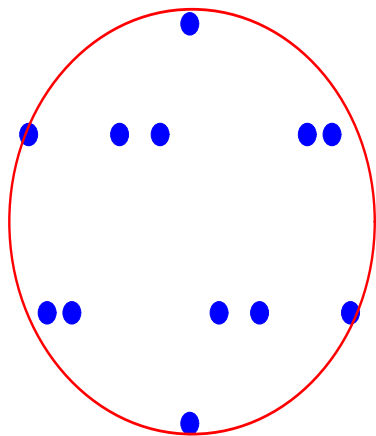


FIG. 16. A schematic diagram for the  $xy$  plane (a) and  $xz$  plane (b) projections of the protein surface charge distribution in DCM model for protein charge  $Z = 12$ .

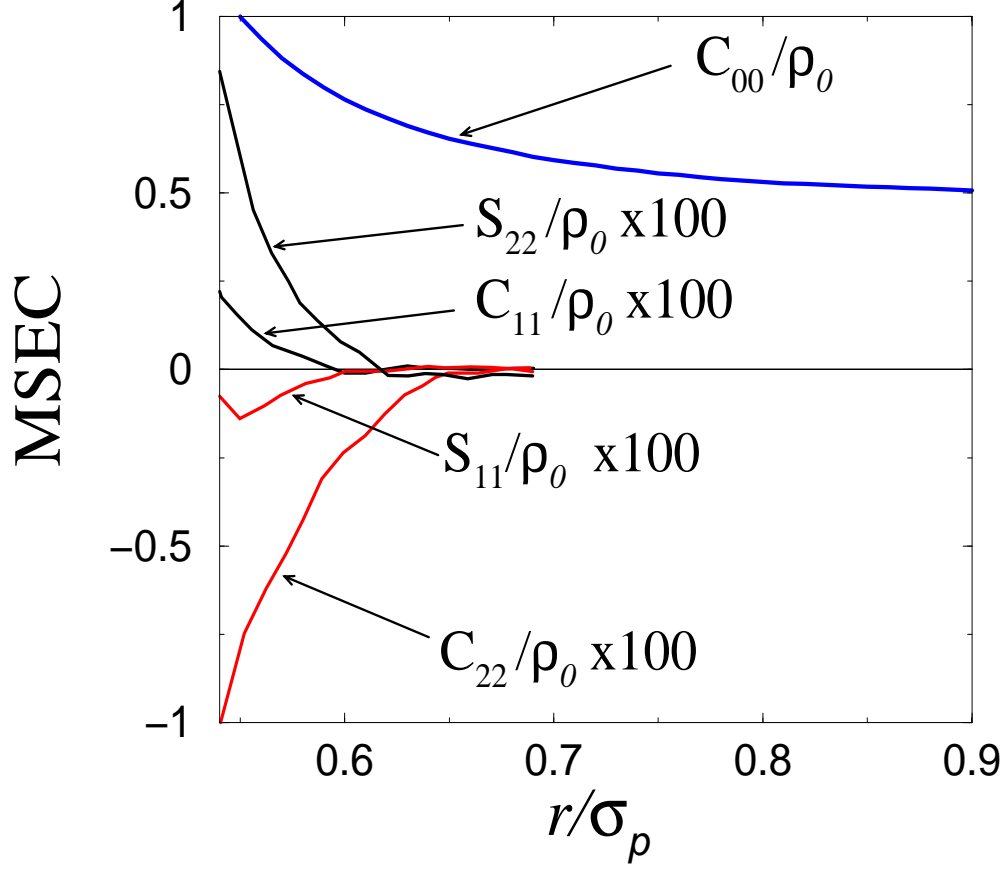


FIG. 17. Five nonzero multipole spherical expansion coefficients (MSEC) of counterion density  $\rho_+(r)$  for the DCM with a protein charge  $Z = 12$  and salt concentration  $C_s = 0.05$  Mol/l. Note that the higher order expansion coefficients are magnified (x100).